JGR Atmospheres

RESEARCH ARTICLE
10.1029/2021JD035749

The Behaviors of Intraseasonal Cloud Organization During DYNAMO/AMIE

Naoko Sakaeda[1] **and Giuseppe Torri**[2]

[1]School of Meteorology, University of Oklahoma, Norman, OK, USA, [2]Department of Atmospheric Sciences, University of Hawai'i at Mānoa, Honolulu, HI, USA

Key Points:

- Currently existing cloud organization indices do not show consistent evolution of intraseasonal cloud organization
- Cloud organization occurs first from an increased number density and proximity, followed by growth in size, then decay in a nonrandom manner
- Intraseasonal cloud organization occurs by modulating the frequency and duration of different stages of mesoscale cloud organization

Correspondence to:
N. Sakaeda,
nsakaeda@ou.edu

Citation:
Sakaeda, N., & Torri, G. (2022). The behaviors of intraseasonal cloud organization during DYNAMO/AMIE. *Journal of Geophysical Research: Atmospheres*, *127*, e2021JD035749. https://doi.org/10.1029/2021JD035749

Received 24 AUG 2021
Accepted 17 MAR 2022

Abstract This study investigates the organization of tropical convection associated with the Madden-Julian Oscillation (MJO) during the Dynamics of the MJO/Atmospheric Radiation Measurement MJO Investigation Experiment field campaign. While it is known that tropical clouds can organize and impact the large-scale environment, how this occurs, and its underlying mechanism are not fully understood. Application of several existing cloud organization indices showed inconsistent evolutions in the measured degree of organization with the MJO. The inconsistency arises from the varying definitions and assumptions of cloud organization behaviors that are applied to each index. While these indices often combine different properties of clouds, such as their number density, size, and distance between them, the analysis of these properties separately provided further understanding of how clouds organize with the MJO. Using the rainfall clusters identified from the S-Polka radar, we find that deep convective rainfall clusters begin to increase their number density before the arrival of MJO enhanced convective center, which is accompanied by increased proximity (shorter distance to each other) and followed by growth in their size. However, the nonrandomness in the spatial distribution of rainfall clusters maximizes as MJO convection decays. Deep convective clusters become the least randomly distributed as the clusters decay because of the suppression and decay of isolated deep convective cells, while clustered deep convective cells exist longer. This evolution of cloud organization is analogous to mesoscale convective systems, indicating that the duration and frequency of their organization stages are altered by the large-scale environmental perturbations associated with the MJO.

Plain Language Summary Tropical cumulus clouds often tend to form close to one another and merge into larger cloud formations with a horizontal dimension greater than 100 km, a phenomenon known as "cloud organization." While we know that cloud organization plays an important role by affecting the surrounding atmosphere through altering humidity and temperature, we do not fully understand why and how clouds organize. This study specifically examines how cloud organization varies on the intraseasonal timescale (30–90 days) that is specifically important to improving long-range prediction skills in the tropics and globally. One finding of this study indicates that we do not have a universally agreed definition of cloud organization that can be used to quantify it, therefore we conduct further analysis to understand how cloud organization occurs. We find that the increased environmental humidity by the MJO first increases the number of cumulus clouds, which naturally leads to their higher proximity, followed by their mergers and growth in size. As the environment dries, scattered and isolated cumulus clouds weaken preferentially, while clustered cumulus clouds live longer, leading to the most "organized" state of clouds. These results show that clouds do not only organize to grow but also to prolong their lifetime.

1. Introduction

The organization of clouds plays important roles in climate and in the dynamics of large-scale tropical variability, such as the Madden-Julian Oscillation (MJO, Madden & Julian, 1994) through its impacts on radiation, surface fluxes, and environmental thermodynamic profiles (e.g., Del Genio & Chen, 2015; Tobin et al., 2012; Wolding et al., 2016). However, the precise definition of cloud organization is unclear, and the term can be used to indicate the formation of mesoscale convective systems (MCSs), the formation of tropical cyclones, self-aggregation in idealized simulations, or any nonrandom distribution of clouds (Muller & Bony, 2015; Retsch et al., 2020; Schumacher & Houze, 2003; Tobin et al., 2012; Tompkins & Semie, 2017; White et al., 2018; Wing et al., 2017). Although several important factors have been identified, such as the environmental humidity and vertical wind shear, cloud-radiative interactions, and the generation of new convection through cold pools (e.g., Cheng et al., 2020; Feng et al., 2015; Holloway & Neelin, 2009; Robe & Emanuel, 2001; Rotunno et al., 1988; Rowe &

Houze, 2015; Torri et al., 2015; Wing & Emanuel, 2014), processes that lead to the organization of clouds are not fully understood. Furthermore, the relative roles of these factors may also depend on the type of cloud organization. Representation of cloud organization and its effects on the large-scale environment in general circulation models (GCMs) are also remaining challenges, which are believed to be key to improving the representation of the MJO in GCMs (Chen & Mapes, 2018; Moncrieff, 2019; Randall et al., 2003; Yang et al., 2019).

Previous studies have improved our understanding of how cloud populations evolve from the convectively suppressed to enhanced state of the MJO. Within the suppressed convective envelopes of the MJO, cloud fraction is low, and most of it is due to shallow, isolated convective clouds. As the state of the MJO transitions from its convectively suppressed to enhanced phase, cloud fraction increases through the increased number of deep convective cells and MCSs with stratiform-anvil clouds (Benedict & Randall, 2007; Genio et al., 2012; Kikuchi & Takayabu, 2004; Powell & Houze, 2015; Xu et al., 2015). While we understand how cloud populations generally evolve with the MJO, we still lack a complete understanding of how the cloud evolution of the MJO fits the definitions of cloud organization and its underlying physical mechanism. This transition from suppressed to enhanced convection of the MJO is often considered to be the transition from unorganized to organized convection, but it is unclear how well the observed behavior follows the existing varying definitions of cloud organization.

Several definitions and indices of cloud organization exist in the literature. Self-aggregation (e.g., Muller & Bony, 2015; Wing et al., 2017) is one type of cloud organization, mostly observed in idealized numerical simulations in radiative-convective equilibrium (RCE), in which the number of clouds reduces to a few large convective systems. Self-aggregation has been studied in observations using indices, such as the Simple Cloud Aggregation Index (SCAI, Tobin et al., 2012) and the Morphological Index of Convective Aggregation (MICA, Kadoya & Masunaga, 2018). These indices consider the number of clouds and their proximity (i.e., the distance between them), and a state with a fewer number of closely distanced convective cloud systems indicate a more aggregated state. Kadoya and Masunaga (2018) found that the MJO suppressed phase is considered to be in a more aggregated state. Other studies, such as Cheng et al. (2018) and White et al. (2018), show that SCAI tends to be a strong function of the number of cloud clusters (i.e., contiguous cloudy/convective areas), which increases within MJO enhanced convection. Therefore, SCAI would also indicate that clouds are more aggregated during MJO suppressed phase when there is a few numbers of clouds. These results suggest that cloud organization associated with the MJO (i.e., its enhanced phase) differs from the description of self-aggregation.

While the aforementioned studies suggest that the MJO is less aggregated during its enhanced phase, other indices would suggest that clouds should be more organized and clustered during the MJO enhanced phase. White et al. (2018) introduced the Cloud Organization Potential (COP) index, which considers the distances between cloud clusters relative to their horizontal sizes. For the pairs of cloud clusters with their centers of mass separated by the same distance, the COP index indicates a higher potential for cloud organization when their sizes are larger. Since the horizontal sizes of cloud clusters are known to increase during the MJO enhanced phase (Xu & Rutledge, 2015; Zuluaga & Houze, 2013), it is expected that the COP index would indicate higher cloud organization potential during MJO enhanced phase. Another organization index was introduced by Tompkins and Semie (2017), which is based on the cumulative density function of distances between nearest-neighboring convective cores and its departure from the cumulative density function of randomly distributed cores. Tompkins and Semie (2017) applied this organization index (I_{org}) to measure clustering of updrafts (i.e., convective cores), while SCAI, COP, and MICA were applied to brightness temperature and outgoing longwave radiation (OLR), where the identified cloud clusters would include anvil clouds surrounding convective cores. Cheng et al. (2018) applied I_{org} to radar data from the Dynamics of the MJO/Atmospheric Radiation Measurement MJO Investigation Experiment (DYNAMO/AMIE) field campaign and showed that 2-day rain episodes from MCSs were associated with clustering of convective cores. Since such 2-day rain episodes and MCSs were more frequent during MJO enhanced phases, their study suggests that convection would be more clustered (organized) during MJO enhanced phases. More recently, Retsch et al. (2020) introduced Radar Organization Metric (ROME), which identifies a higher degree of organization when there is a larger spread in sizes and/or the proximity of clouds is higher. Since ROME generally increases with increased size of convective clouds, it would also likely identify the MJO enhanced phase to be more organized than the suppressed phase.

These prior studies suggest that cloud organization associated with the MJO may be diagnosed differently depending on the choice of cloud organization indices. The organization indices discussed here combine multiple factors (e.g., number, sizes, distances) to diagnose the state of organization, which makes it difficult to fully understand

which factors contribute to the organization. Some of the indices, such as SCAI, are intended to capture cloud organization behaviors that appear in idealized model simulations, but we do not have a complete understanding of how clouds organize based on observations. Therefore, the objectives of this study are (a) to examine the applicability of existing cloud organization indices to the MJO, and (b) to provide an extended analysis of how cloud organization evolves with the MJO using DYNAMO/AMIE field campaign observations.

2. Data and Methods

2.1. Observations During DYNAMO/AMIE

We will use data from the S-Polka radar to identify and quantify the organization of precipitating cloud populations, which was deployed at 0.63°S and 73°E in Addu Atoll, Maldives between October 1, 2011 and January 16, 2012. S-Polka is a dual-polarized, dual-wavelength radar with S-band and Ka-band that had 15-min scan cycle that includes full horizontal (PPI) and vertical (RHI) scans over some selected range. More information about the field campaign and radar scanning strategies are summarized in Yoneyama et al. (2013).

The radar data are gridded to 1 km horizontal and 0.5 km vertical grids within 150 km radius domain, which is available from its Legacy website (http://dynamo.fl-ext.ucar.edu/rsmas/dynamo_legacy/). Near-surface rain rates are estimated using an algorithm that utilizes relationships with differential reflectivity and derived specific differential phase from Thompson et al. (2018) for S-Polka. Rain types were identified by an algorithm developed by Powell et al. (2016) that uses the intensity and horizontal extent of echo at 2.5 km altitude to classify rain types into deep convective, stratiform, mixed (both deep convective and stratiform), isolated convective core and fringes, and weak echo. Strongest radar echoes that exceed a background threshold value are defined as deep convective and their adjacent echoes are defined as mixed and stratiform for large echo objects. Smaller echo objects are classified as isolated convection and weak echo depending on their reflectivity. More information on the method for processing and deriving rain rate estimates, their uncertainty, and rain types are described in Dolan et al. (2017).

In addition to the DYNAMO ground-based radar, half-hourly, 4 km gridded NOAA NCEP/NPC merged IR brightness temperature (Janowiak et al., 2017) is used to evaluate cloud organization. As discussed in Section 1, some of the cloud organization indices were developed to be used with brightness temperature data, which provides estimates of cloud top heights. We will use both brightness temperature and ground-based radar data to test the sensitivity of cloud organization indices to the resolution and choice of variables.

Environmental profiles will be examined using the Colorado State University (CSU) upper-air and surface gridded analysis (Ciesielski et al., 2014) that provides 3-hourly, 1° horizontal and 25 hPa vertical resolution thermodynamic and kinematic variables from October 1 to December 31, 2011. This CSU gridded data includes inputs from the 3-hourly radiosonde launches at Gan Island of Addu Atoll.

2.2. Identification of MJO Phase

The evolution of the MJO over Addu Atoll is identified using 12-hourly, 2.5° gridded NOAA interpolated OLR (Liebmann & Smith, 1996), a commonly used variable to estimate MJO convectively activity, that is available from 1979 to the present. OLR anomaly is first calculated by removing its mean and the first three harmonics of the seasonal cycle. OLR anomalies are then filtered for MJO wavenumber-frequency band (20–100 days, 1–10 eastward zonal wavenumber) following the method of Wheeler and Kiladis (1999) that uses the inverse Fourier transform coefficients of the selected wavenumber-frequency band.

The local state of the MJO is determined by the phase diagram defined by the MJO-filtered OLR anomaly and its time tendency (e.g., Riley et al., 2011; Sakaeda et al., 2020; Yasunaga & Mapes, 2011). Local phase angles 0° and ±180° define the center of MJO enhanced and suppressed phases, respectively. A positive phase angle indicates the period of transition from MJO suppressed to enhanced phase (growing phase), while a negative phase angle indicates the opposite (decaying phase). This local phase identifies the state of the MJO over Addu Atoll, which is an advantage over global EOF-based indices, such as the Real-time Multivariate MJO index (RMM, Wheeler & Hendon, 2004) or OLR MJO Index (OMI, Kiladis et al., 2014), that do not necessarily capture the regional state of the MJO. Figure 1a shows the local MJO phase during DYNAMO/AMIE over Addu Atoll, capturing the observed three MJO events (Yoneyama et al., 2013). We examine the evolution of cloud organization and

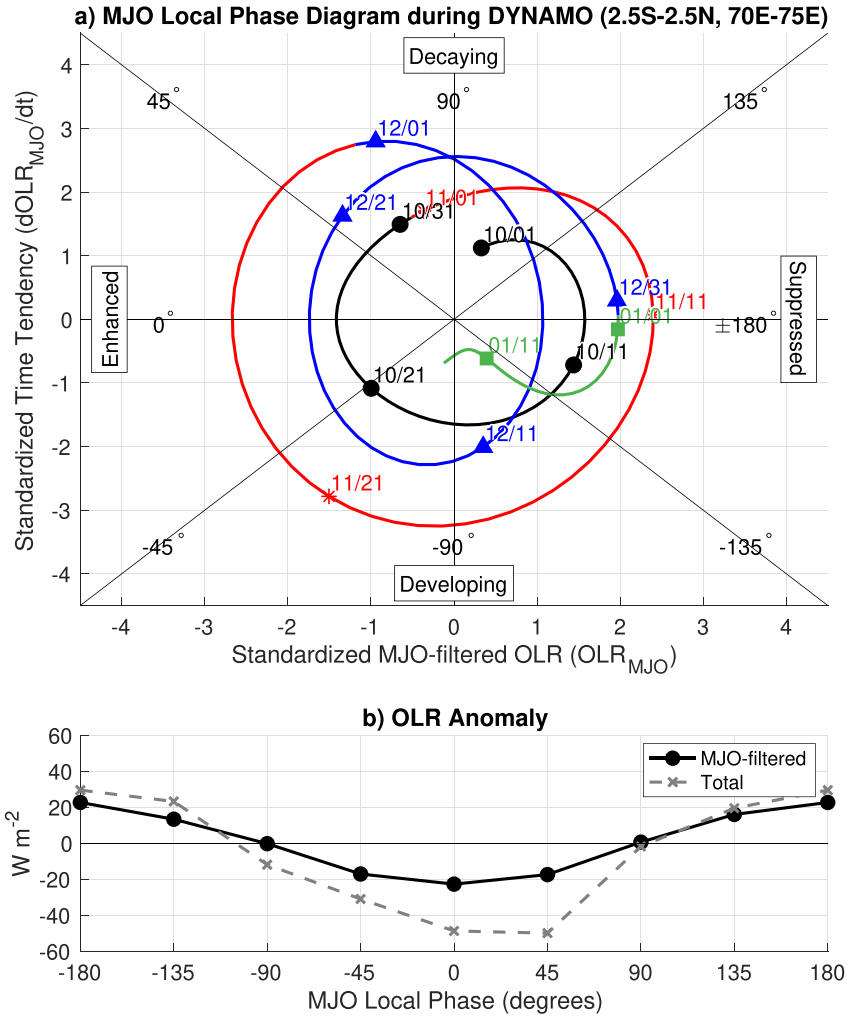

Figure 1. (a) Evolution of MJO local phase diagram during DYNAMO from October 1, 2011 to January 15, 2012 based on MJO-filtered OLR anomalies averaged from 2.5°S to 2.5°N and 70°−75°E. (b) Composite of total and MJO-filtered OLR anomalies by MJO local phase during DYNAMO.

other quantities of interest by compositing them based on this MJO local phase. Figure 1b shows an example with MJO-filtered OLR anomalies, which, by construction, minimize and maximize at MJO local phases of 0° and ±180°, respectively. Total OLR anomalies minimize at local phase 0–45°. The continuous minimum in total OLR anomalies at 45° indicates the persistence of high clouds and their following rapid decay. Throughout the manuscript, all statistical significances are tested using a 1,000-iteration bootstrap resampling with repetition and 95% confidence level.

2.3. Cloud Organization Indices

Figure 2 shows examples of rain and cloud clusters that are used to calculate cloud organization indices. Throughout this manuscript, a "cloud cluster" is defined as a contiguous area (using 4-neighbor method) of brightness temperature below some threshold values (Figure 2d). A "rain cluster" is defined as a contiguous area of nonzero near-surface rain rate, identified using S-Polka rain estimates (Figure 2e). Using the rain type classifications by the algorithm of Powell et al. (2016), rain clusters can also be separated into two types: MCSs that are defined as large clusters composed of deep convective, mixed, and stratiform rain types and sub-MCSs that contain all other smaller clusters. A "convective rain cluster" is identified as a contiguous area of raining pixels classified as deep convection (Figure 2f). To calculate cloud organization indices, the number of rain or cloud clusters, their horizontal sizes, and distances between each pair of clusters are recorded at every 15 or 30 min, depending

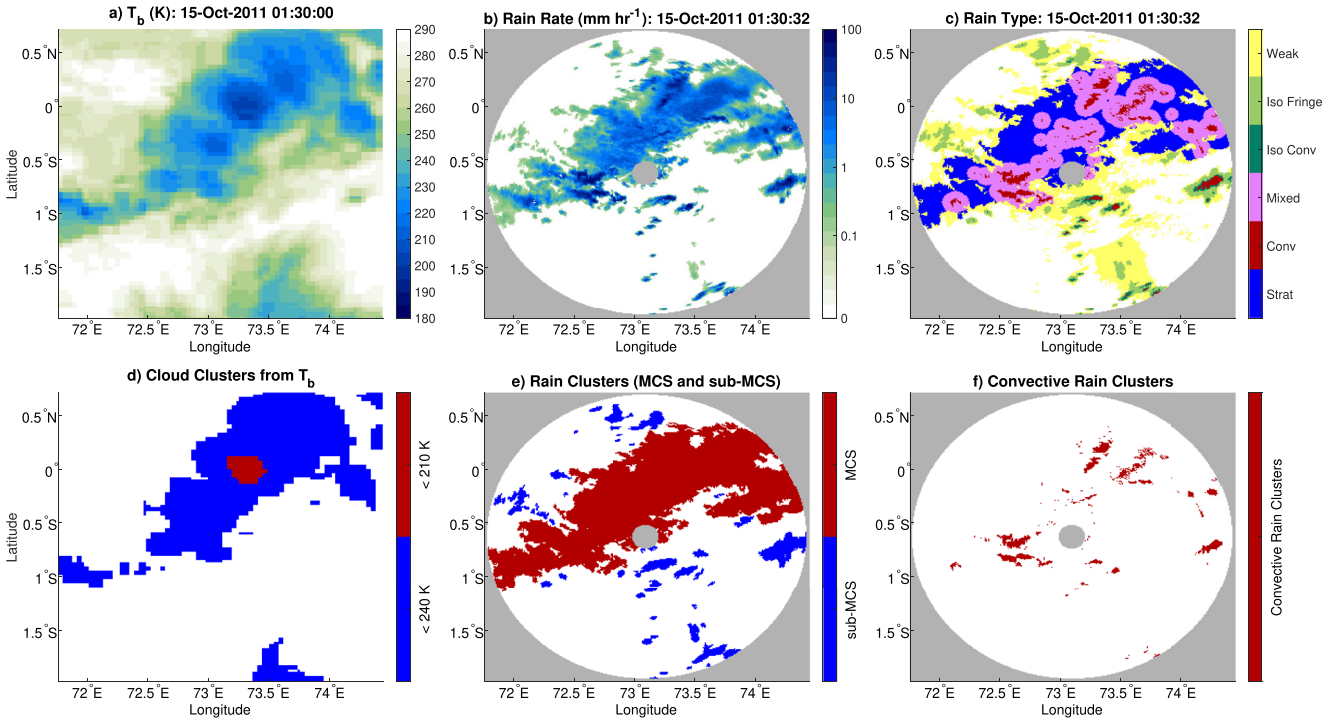

Figure 2. Examples of (a) brightness temperature (k), (b) rain rate (mm hr^{-1}), and (c) classified rain types showing stratiform (blue), deep convective (red), mixed (magenta), isolated convective core (dark green), isolated convective fringes (light green), and weak echo (yellow) around 01:30 UTC October 15, 2011. (d) Identified cloud clusters using 210 K (red) and 240 K (blue) brightness temperature. (e) Identified rain clusters that can be separated into MCSs (red) and sub-MCSs (blue, see text for their definitions). (f) Convective rain clusters.

on the resolution of the data. Distances between rain or cloud clusters are defined as the distances between their geometric centroids. Cloud organization indices are calculated at each instantaneous time using the identified rain clusters and convective rain clusters within the radar domain and with cloud clusters identified within a 5° × 5° box centered over Addu Atoll.

Throughout the manuscript, we will use different words to describe cloud organization and its indices. As summarized in Table 1, we use "aggregation" to describe the evolution of cloud populations toward a state of a fewer and larger convective cloud systems that is often observed in idealized RCE simulations. "Clustering" will be used to describe a state where cloud populations become more closely distributed, while "nonrandomness" describes a state where clouds are more closely located than their expected random distribution. We consider "organization" as a term without a specific definition, but it generally describes changes in the characteristics of cloud populations from suppressed to enhanced state of convective activity.

2.3.1. Simple Cloud Aggregation Index, SCAI

The Simple Cloud Aggregation Index (SCAI, Tobin et al., 2012) is defined as:

Table 1
Description of Terminology Related to Cloud Organization

Term	Definition
Aggregation	Change in cloud populations toward a state with a reduced number of larger convective systems
Clustering	Change in cloud populations toward a state with decreased distance between them
Nonrandomness	A state where the distances between objects (e.g., clouds) are closer than the distances expected if the same number and size of the objects are distributed randomly
Organization	A process that occurs as convective activity transitions from its suppressed to enhanced state, which can broadly encompass aggregation, clustering, nonrandomness, or other changes in cloud properties

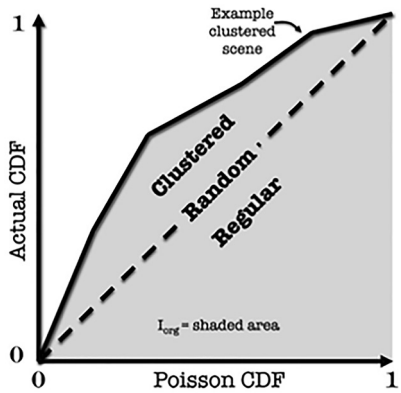

Figure 3. An example of actual NNCDF plotted against $NNCDF_{random}$. I_{org} is defined as the integral under the curve. Figure adapted from Figure 18 in Tompkins and Semie (2017).

$$SCAI = 1,000 \times \frac{N}{N_{max}} \frac{D}{L}, \quad (1)$$

where N is the number of clusters, N_{max} is the maximum potential number of clusters that is calculated as half the number of total grid points, D is the geometric mean of the distance between the centroid points of all cluster pairs, and L is the length of the domain. A smaller value of SCAI indicates a more aggregated state as the number of clusters and their distances decrease.

2.3.2. Organization Index, I_{org}

The Organization Index (I_{org}, Tompkins & Semie, 2017) diagnoses the degree of nonrandomness using distances between each cluster and its nearest neighbor. The cumulative distribution of nearest-neighbor distances (NNCDF) is compared to the cumulative distribution of randomly distributed clusters ($NNCDF_{random}$) that is represented as a Weibull distribution:

$$NNCDF_{random}(d) = 1 - \exp\left(-\lambda \pi d^2\right), \quad (2)$$

where d is the distance between the centroid points of nearest-neighboring clusters and λ is the number of clusters per unit area. I_{org} is defined as the integrated area under actual and random NNCDF (Equation 3) as illustrated in Figure 3:

$$I_{org} = \sum NNCDF(d)\left[NNCDF_{random}(d + \delta d/2) - NNCDF_{random}(d - \delta d/2)\right]. \quad (3)$$

To find a discrete NNCDF, nearest-neighboring distances are binned using the diagonal distance of the horizontal grid resolution as the uniform width of bins (e.g., $\delta d = 1.41$ km for 1 km grids). If the clusters are randomly distributed, the actual and random NNCDF have a one-to-one relationship, which makes I_{org} be equal to 0.5. When the clusters are closer together than when randomly distributed, I_{org} would be greater than 0.5. This index measures organization as the degree of deviation from a random distribution (nonrandomness). Therefore, the average physical distance between nearest-neighboring clusters can be different even under the same I_{org} value depending on the number density of the clusters. This index also assumes that cluster sizes are small and uniform, which is applicable for identifying the clustering of convective updrafts as done by Tompkins and Semie (2017).

2.3.3. Morphological Index of Convective Aggregation (MICA)

The Morphological Index of Convective Aggregation (MICA, Kadoya & Masunaga, 2018) diagnoses aggregation based on the concentration of cloud clusters, and it is defined as

$$MICA = \frac{\sum_{i=1}^{N} S_{cls,i}}{A_{cls}} \frac{(A_{obs} - A_{cls})}{A_{obs}}, \quad (4)$$

where A_{obs} is the total observed area, A_{cls} is the area of the smallest possible rectangle that encloses all cloud clusters within the domain, $S_{cls,i}$ is the area of the ith cloud or rain cluster. The first fraction $\left(\sum_{i=1}^{N} S_{cls,i}/A_{cls}\right)$ quantifies the density of clusters within the cloudy or rainy region, and the second fraction $((A_{obs} - A_{cls})/A_{obs})$ quantifies the fraction of clear area. As clusters are more concentrated into a smaller area (i.e., more aggregated), the value of MICA increases. For the application of this metric to a radar domain, A_{cls} was calculated as the smallest possible circle (instead of a rectangle) that encloses all clusters.

2.3.4. Convective Organization Potential (COP)

The Convective Organization Potential (COP, White et al., 2018) diagnoses cloud clustering based on the distances between the centroid points of cloud or rain clusters relative to their sizes. White et al. (2018) define Interaction Potential V as:

$$V(i,j) = \frac{\sqrt{A_i} + \sqrt{A_j}}{\sqrt{\pi} d(i,j)} = \frac{r_i + r_j}{d(i,j)}, \tag{5}$$

where A_i and A_j are the areas of two objects whose centroids are separated by distance $d(i, j)$. The approximate radii of the clusters are $r_i = \sqrt{A_i/\pi}$ and $r_j = \sqrt{A_j/\pi}$. COP is then defined as the mean interaction potentials (Equation 6), which would have higher values when objects are closer relative to their sizes (i.e., more clustered).

$$\text{COP} = \frac{\sum_{i=1}^{N} \sum_{j=i+1}^{N} V(i,j)}{(1/2)N(N-1)}. \tag{6}$$

2.3.5. Radar Organization Metric (ROME)

The Radar Organization Metric (ROME, Retsch et al., 2020) defines a scalar c for each unique pair of clusters. The scalar c is the sum of the area of the larger cluster, A_a, and its smaller cluster, A_b, weighted by its ratio to the area of the smallest square that fits between their edges, A_d (Equation 7):

$$c = A_a + \min\left(1, \frac{A_b}{A_d}\right) \cdot A_b. \tag{7}$$

When there is more than one cluster, ROME is calculated by finding the average of c, whereas if there is only one cluster, ROME equals the area of the single cluster (Equation 8):

$$\text{ROME} = \begin{cases} \frac{1}{k} \sum_{i=1}^{k} c_i, k = (1/2)N(N-1) & \text{for } N > 1 \\ A_a & \text{for } N = 1 \end{cases} \tag{8}$$

ROME is developed based on the assumption that a more organized state has larger clusters. ROME increases when the sizes of clusters increase and/or when their proximity increases. ROME can also be decomposed as $\text{ROME} = \bar{A} + \Delta_{size} + \Delta_{prox}$, where $\bar{A}$ is the mean area of all clusters and it is the lower bound of ROME (R_{min}). Δ_{size} relates to the spread in sizes, which is defined as the difference between R_{min} and a noninteractive ROME value (R_{NI}) that is obtained by assuming that A_d is infinity. Δ_{prox} is the difference between ROME and R_{NI}, which relates to proximity (distances) between the clusters.

3. Evolution of Cloud Organization Indices

This section will show the evolution of the five cloud organization indices introduced in Section 2.3 associated with the three MJO events observed during DYNAMO/AMIE. We will demonstrate that which MJO phase has more "organized convection" varies significantly depending on the choice of indices, since each index emphasizes a different aspect of cloud organization characteristics.

Figures 4a and 4b show the average evolution of domain-mean S-Polka rain rates and brightness temperature based on MJO local phase that is divided into eight phases (every 45°). Rainfall maximizes slightly before the center of MJO enhanced convection (i.e., before MJO local phase of 0°) and the brightness temperature minimizes slightly after (consistent with total OLR anomaly in Figure 1b). This lag of OLR and brightness temperature minima following rainfall maximum is observed in prior studies (e.g., Ciesielski et al., 2017; Kiladis et al., 2005), and it suggests the presence of high, weakly or nonprecipitating clouds following the peak of deep convection.

Figures 4c–4l show the evolution of the five cloud organization indices discussed in Section 2.3. Smaller SCAI values indicate a more aggregated state while other indices indicate more aggregated or clustered states when their values are larger. To facilitate comparison between the indices, the vertical axis of SCAI (Figures 4c and 4d) is reversed (smaller value at the top), and the vertical axes of each panel are different. The organization indices are calculated using rain clusters (both MCSs and sub-MCSs) and convective rain clusters of S-Polka, and using cloud clusters identified using 240 and 210 K thresholds of brightness temperature. SCAI indicates that the MJO is generally more aggregated during the suppressed phase (~135–180°) than the enhanced phase (~−45° to 0°), regardless of the choice of variable and thresholds. Previous studies have shown that SCAI is largely dependent on the number of clusters (Cheng et al., 2018; White et al., 2018), which increases during MJO enhanced

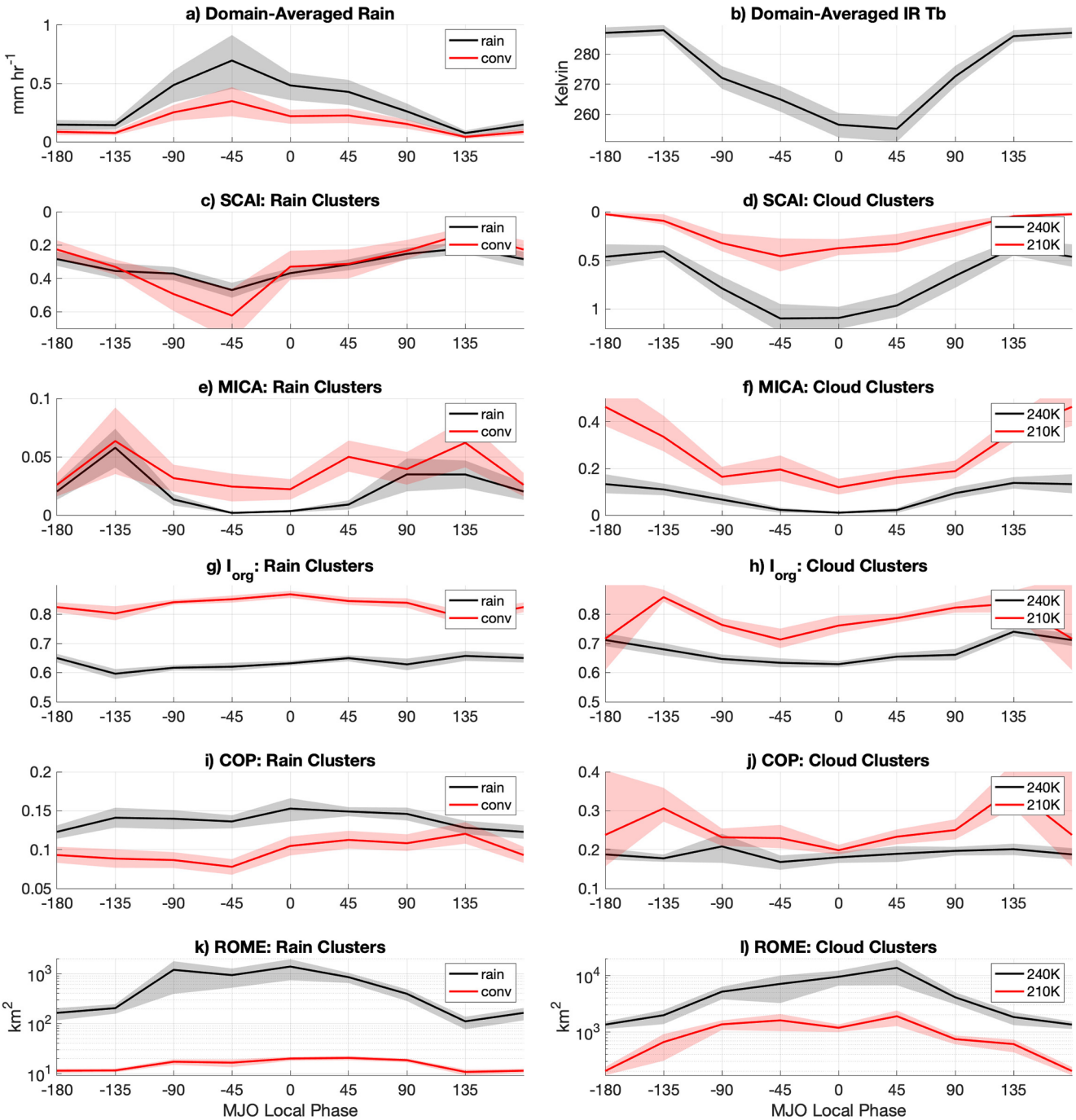

Figure 4. MJO local phase composites of S-Polka rain rate, IR brightness temperature, and organization indices. (a) S-Polka domain-averaged total (black) and convective (red) rain rate. (b) Area-averaged brightness temperature within 5° box centered at the location of S-Polka. (c–j) SCAI, I_{org}, MICA, and COP calculated using S-Polka rain clusters (black) and convective rain clusters (red) on the left column and the same indices calculated using cloud clusters identified using brightness temperature thresholds of 240 K (black) and 210 K (red) on the right column. Shading shows the 95% confidence interval in the composite values.

phase, leading to larger SCAI values (less aggregation). Figures 5a and 5b also show that SCAI generally follows the number density of clusters. When SCAI is calculated separately for MCS and sub-MCS rain clusters, its values still maximize (least aggregated) during MJO enhanced phase due to their increased number (not shown). Geometric mean distances between the centroid points of clusters (D, Figures 5c and 5d) also tend to increase during MJO enhanced phase due to the growth in the size of clusters. Since SCAI uses the mean distance of all unique pairs of clusters, an increased number of clusters can also increase the mean distance. As the number

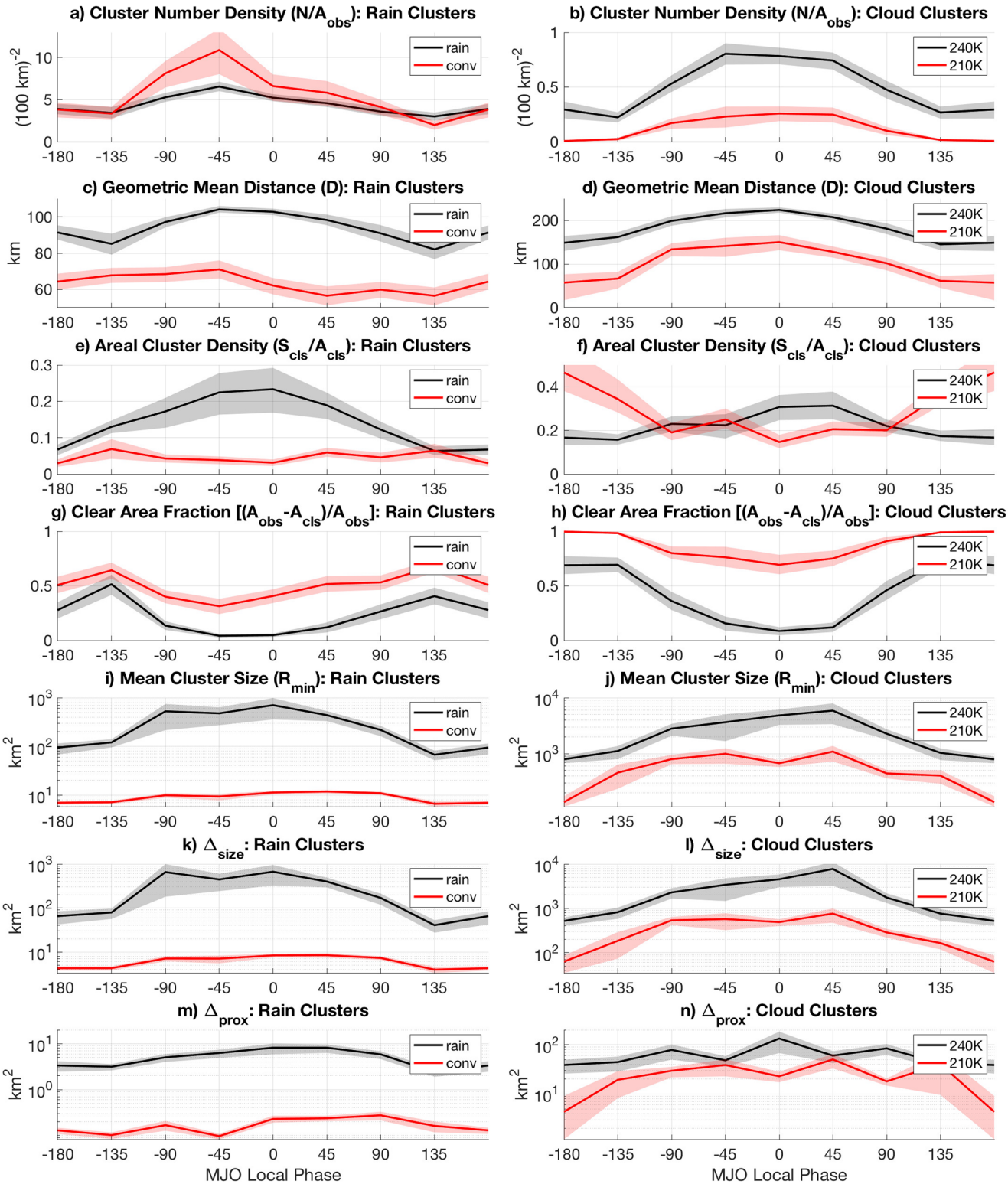

Figure 5. MJO local phase composites of parameters that are included in cloud organization indices shown in Figures 4a and 4b. Number density of clusters (per 10^2 km^2), (c, d) geometric mean of distances between all cluster pairs, (e, f) areal cluster density (S_{cls}/A_{cls}), (g, h) clear are fraction $[(A_{obs} - A_{cls})/A_{obs}]$, (i, j) mean cluster size (R_{min} or $\bar{A}$, km^2) (k, l) a measure of spread in size (Δ_{size}, km^2), and (m, n) a measure of cluster proximity (Δ_{prox}, km^2)). Left column shows rain clusters and right column shows cloud clusters.

increases, some pairs are expected to be separated by a greater distance even though the distance between nearest-neighboring clusters might be decreasing.

MICA is also designed to capture self-aggregation and it also generally minimizes during the MJO enhanced phase (i.e., less aggregation). This is consistent with the results of Kadoya and Masunaga (2018) who found that the MJO is more aggregated during its suppressed phase. MICA appears to be dominated by the fraction of overall clear area [$(A_{obs} - A_{cls})/A_{obs}$, Figures 5g and 5h], which minimizes during MJO enhanced phase as expected. The density of clusters within the overall cloudy area (S_{cls}/A_{cls}, Figures 5e and 5f) increases during MJO enhanced phase based on rain clusters or cloud clusters with higher brightness temperature threshold. However, based on convective rain clusters or cloud clusters with lower Tb thresholds, their density minimizes during the MJO enhanced phase. These results demonstrate that this organization index depends on how the clusters are defined (e.g., deep convective cores vs. overall cloudy area). Since the total area of convective rain (S_{cls}) is higher during the MJO enhanced phase (Figures 5a and 5b), the smallest area that encloses all clusters (A_{cls}) must be increasing during the MJO enhanced phase. This suggests that there are groups of deep convective clusters that form within the MCSs during MJO enhanced phase. As MCSs develop, these groups of convective cores within each MCS must be separated by the size of each MCS, leading to increased A_{cls}. Similarly to SCAI, MICA suggests that cloud organization during MJO enhanced phase is not consistent with the behavior of self-aggregation.

The other indices, I_{org}, COP, and ROME show a different evolution and they are more sensitive to the choice of variables, thresholds, and how clusters are defined. I_{org} based on convective rain clusters indicate that they become more clustered and nonrandom during MJO enhanced phase, while a clear trend is not seen from I_{org} that is calculated with rain clusters (even when separated to MCSs and sub-MCSs, not shown). This is because this index is more applicable to small objects of similar size, but rain clusters can vary in size greatly. Figure 6b shows how the distribution of rain cluster size changes with the MJO. Shadings in Figure 6b show anomalous probability of rain cluster sizes, where positive and negative anomalies indicate increased or decreased probabilities of observing the particular size of rain clusters. During MJO enhanced phase, sizes of rain clusters bifurcate, where clusters of size greater than 100 km^2 and smaller than 20 km^2 become more frequent, possibly due to an increased chance of merging of rain clusters with sizes greater than 100 km^2. This also leads to bifurcation of nearest-neighboring distances (NND) as shown in Figure 6d, since the distance between the centroid points of clusters must increase when their sizes increase. When there is a large variability in the sizes of rain clusters, the interpretation of I_{org} becomes difficult because the random distribution of clusters with varying sizes cannot be well represented by Equation 2. When I_{org} is applied to convective rain clusters whose sizes are less variable (Figure 7b), their NND distributions decrease during MJO enhanced phase (Figure 7d), leading to higher I_{org} values.

COP considers the distances between rain/cloud clusters relative to their sizes. COP based on rain clusters indicate that their distances become smaller relative to their sizes (Figure 4i), which suggests a higher organization potential (V). However, COP based on "convective" rain clusters or cloud clusters indicate that they are farther away relative to their sizes as the MJO develops into its enhanced phase (Figures 4i and 4j). Figure 6c shows that the distance between all unique pairs of rain clusters tends to maximize during MJO enhanced phase. Figure 6e shows the normalized distances of each pair of clusters divided by the sum of their radii, $[d(i, j)/(r_i + r_j)]$, which is the inverse of Interaction Potential V that is considered in COP. During MJO enhanced phase, the normalized distance of rain clusters bifurcate with increased probability of the normalized distance less than 10 and greater than 50. The increased probability of smaller normalized distance leads to an increase in COP, but only a small increase in COP is observed (black line in Figure 4i) due to the offset by the increased probability of large normalized distances. This increased probability of large normalized distances occurs because of the increased number of clusters (Figure 5a). COP considers the distances of all unique pairs of clusters (not just nearest-neighboring distances as in I_{org}), so even if the nearest-neighboring clusters become closer to each other during MJO enhanced phase, the distances between some pairs of clusters must increase, thus favoring lower COP values. The same explanation can be applied to understand lower COP values during MJO enhanced phase using convective rain clusters or cloud clusters. As shown in Figure 7e, normalized distances of convective rain clusters increase when their numbers increase, leading to lower COP values (less clustered as shown by the red line in Figure 4i).

Lastly, ROME uniquely quantifies cloud organization that also depends on the size of cloud/rain clusters. ROME is not dimensionless, so its value highly depends on the choice of data and how clusters are classified. Although the magnitudes are different, Figures 4k and 4l show that ROME based on either rain or cloud clusters maximizes during the MJO enhanced phase (i.e., increased organization). As Retsch et al. (2020) showed, ROME can be

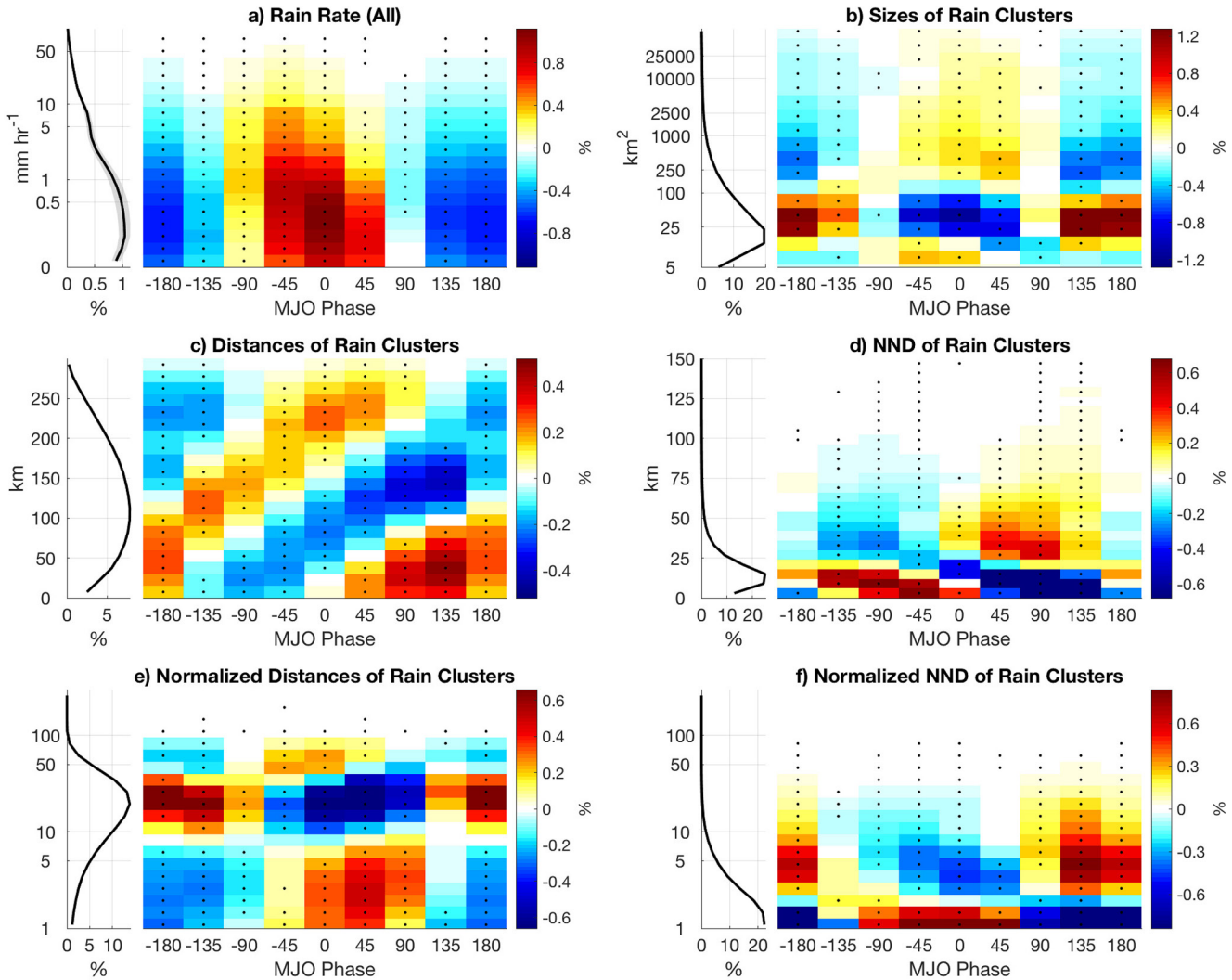

Figure 6. Probability distribution of S-Polka rain rates and properties of rain clusters identified using all rain types. Black line at the left of each panel shows the probability distribution during all local phases of the MJO (i.e., distribution during DYNAMO). Shading shows anomalous probability distribution at each MJO local phase from the DYNAMO distribution. Black dots indicate that the anomalous probabilities are statistically significantly different from zero. (a) Probability distribution of rain rates, (b) sizes of rain clusters, (c) distances between all unique pairs of rain clusters, (d) nearest-neighboring distances (NND) of rain clusters, (e) normalized distances (distances divided by the sum radii of cluster pair), (f) normalized NND (NND divided by the sum radii of NND pairs).

decomposed to $\bar{A}$ (or R_{min}), Δ_{size}, and Δ_{prox} that are shown in Figures 5i–5n. The evolution of ROME with the MJO is mainly contributed by $\bar{A}$ and Δ_{size}, where the increase in the average size of clusters and the wider distribution of their sizes contribute to the increase in ROME. The contribution from Δ_{prox}, which is based on the proximity of clusters, is at least an order of magnitude smaller than the other terms, but it captures increased proximity (clustering) following the maximum in $\bar{A}$ and Δ_{size}.

The comparison of these cloud organization indices revealed that no consistent degree of cloud organization associated with the MJO can be diagnosed. One reason for the discrepancies is that these indices include different sets of input parameters and their weighting functions based on varying underlying definitions of cloud organization (Table 2). However, the combination of these indices and the assessment of their input parameters have revealed a few behaviors of cloud organization associated with the MJO. As the large-scale environment transitions from suppressed to enhanced MJO phase, (a) rain and cloud clusters increase in their number. (b) While some clusters grow in size, the number of small cells also increases. (c) The distances between the nearest-neighboring clusters also decrease relative to their sizes. Prior studies have also shown some of these points separately (Barnes & Houze, 2013; Feng et al., 2015; Powell, 2019), but the analyzed cloud organization indices do not capture

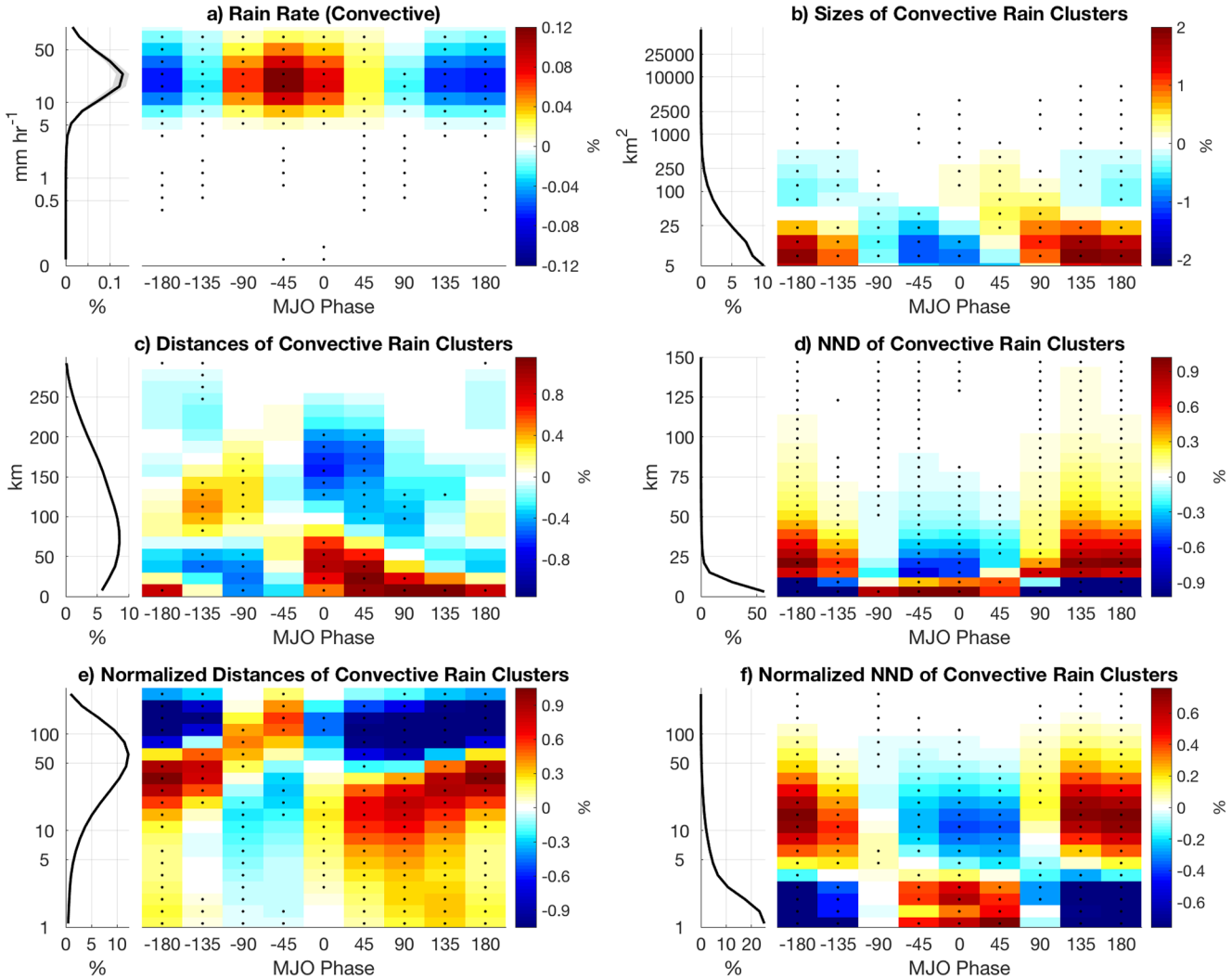

Figure 7. Same as Figure 6 except showing probability distributions of convective rain rates and convective rain clusters.

these behaviors single-handedly. Table 2 summarizes that these indices may be useful for diagnosing the state of organization in a simple manner, for example, for model evaluation purposes, but caveats associated with them need to be carefully considered. These indices also consider the average or distribution of different properties of rain/cloud clusters (e.g., size, number, distance), so the indices tend to be dominated by the type of clusters that are dominant in number. For example, for rain clusters, their cloud organization indices tend to be dominated by sub-MCSs that comprises over 95% of the total number of rain clusters (not shown). The behaviors of cloud organization can be oversimplified by the use of organization indices that take average characteristics of rain/cloud clusters that do not have normal distributions as shown in Figures 6 and 7. The challenges of developing cloud organization indices relate to our incomplete understanding of cloud organization behaviors and processes. Therefore, the remainder of this study will focus on providing greater depth of observational analysis to understand the characteristics associated with cloud organization.

4. Observed Behavior of Cloud Organization

The previous section showed how the number, size, and distances between rain and cloud clusters evolve as the MJO transitions from suppressed to enhanced phase. These properties of rain and cloud clusters are also related to each other to some extent. For example, if there is a greater density of clusters, their proximity must increase (even for a random distribution), as does the chance of merging to grow in size. These behaviors are also

Table 2
Summary of Cloud Organization Indices

Index	Implied definition of cloud organization	Strength	Caveats
SCAI	A state of smaller number and more closely distanced clouds	It provides a simple measure of "self-aggregated" state that appears in idealized simulations	It is strongly dependent on the number than the distances between objects. Observed states of enhanced convection and organization often have higher number of clouds, contradicting the definition of cloud organization by SCAI
*I*org	A state where convective cells are more closely distributed than a random distribution	Provides a simple measure of how the observed distribution of objects compares to a random distribution of points	It is only applicable to objects that can be assumed to have relatively small and uniform sizes (e.g., deep convective cells)
MICA	A state of greater clear-sky area while clouds are densely populated in a smaller region	It provides an another measure of "self-aggregation" that also considers the distribution density of clouds	It is dominated by the fraction of clear-sky area, which often maximizes during suppressed convective states in observation
COP	A state of clouds that are closely distanced relative to their sizes	For two objects whose centroids are separated by the same distance, it accounts for their size variability that influences their chance of interaction	The index considers the proximity between all unique pairs of objects. Therefore, even when the nearest-neighboring objects are separated by the same distance, the measured proximity by this index decreases when there is a large number of objects
ROME	A state where clouds are larger in size and more closely distanced	It allows to decompose the contributions from average size, spread in size, and proximity. It can also be quantified when there is one object	The index is not dimensionless, making it highly sensitive to the choice of variables. The contribution from size tends to dominate over proximity

associated with the evolution in the type of clouds and rainfall. The growth in size is associated with increased stratiform-anvil clouds, while the greater spread in size is also contributed by increased formation of isolated convection. This section will examine how these behaviors of rain clusters relate to each other, in order to better understand the behavior of cloud organization. The remainder of this study focuses on the analysis of S-Polka radar, which provides rain type classification and allows us to examine the evolution of different rain types.

In addition to the number, size, and distances between rain clusters analyzed in Section 3, an additional property that is relevant to understanding cloud organization is how the distribution of rain clusters compares to an expected random distribution (nonrandomness of rain cluster distribution). We will quantify the degree of nonrandomness by modifying I_{org}. I_{org} measures how the distribution of NND of clusters deviates from a random distribution expected for a Poisson point process (Tompkins & Semie, 2017; Weger et al., 1992), which is applicable when we can assume that rain clusters have relatively small and uniform sizes. However, as demonstrated in Section 3, rain and cloud clusters vary significantly in sizes and there is no analytical equation for their random NNCDF. Therefore, we will measure the true departure of rain clusters from their random distribution by following a method similar to Nair et al. (1998), which calculates a random NNCDF by simulating a random distribution of observed clusters. We relocate rain clusters by randomly selecting their centroid location while avoiding overlaps with other clusters. An example of such random relocation is shown in Figures 8a and 8b. This relocation was done in the order of the largest to smallest clusters to maximize the chance of relocating all clusters without overlaps. The randomization process may stop when there is no domain left to fit a rain cluster without overlap, which only occurs when raining area fraction is close to 100%. If the randomly selected location of the centroid is close to the edge of the radar domain, a cluster may be partially cut off. To eliminate the effect of these cases where the exact number and shape cannot be retained through the randomization process, the process is repeated 100 times for each 15-min radar scan, generating 100 samples of the randomized rain clusters. This process provides an expected distribution of NND from randomized clusters (Figures 8e and 8f), while retaining the observed number, orientation, and shapes of clusters (Figures 8c and 8d). The 100-iterations of this randomization also provides a spread in the randomized NNCDF, which can be compared with actual NNCDF to measure its true departure from random distribution and its confidence interval. Our objective here is to quantify the degree of nonrandomness in rain cluster distribution, instead of advocating for a new cloud organization index.

Figures 9a–9d show the distributions of the observed and randomized NND of rain clusters and convective rain clusters within each local MJO phase. For the randomized clusters, all 100-iterations from each radar scan are included to generate the distribution of NND. The distances between the observed clusters tend to be shorter than

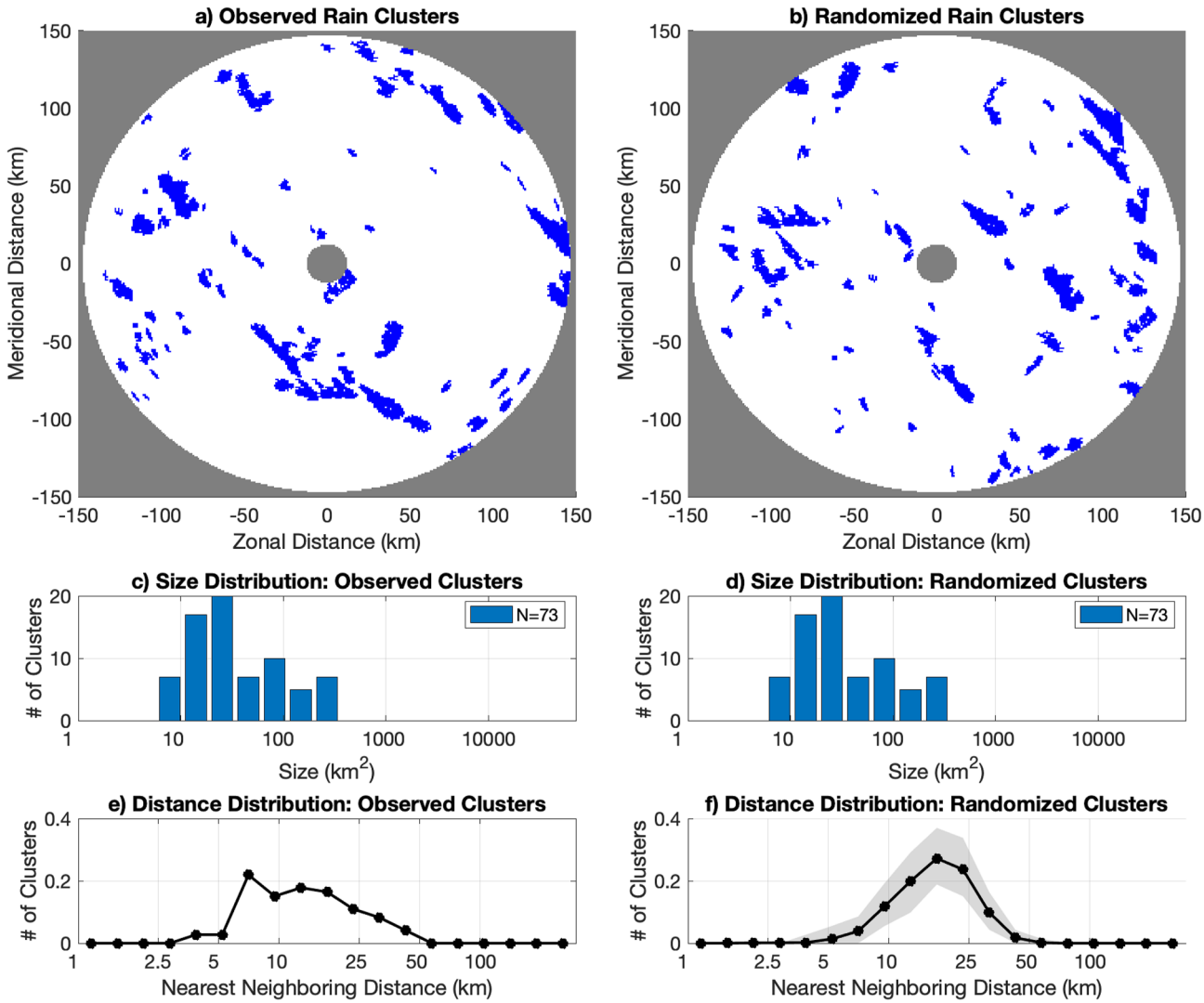

Figure 8. An example of (a) observed rain clusters and (b) randomized clusters. (c, d) Observed and randomized size distributions. (e, f) Distributions of nearest-neighboring distance (NND) of observed and randomized clusters. Gray shading in panel f shows the 95% confidence interval that is generated by repeating the randomization for 100 times.

the randomized distances. For convective rain, the difference between observed and randomized NND is greater, indicating that the distribution of deep convection rarely appears as a purely random distribution. The NND of rain clusters minimizes slightly ahead of MJO enhanced convection center (around −45° to 0°). This increased proximity of clusters also occurs for randomized clusters at the same phase due to the maximum number of the observed cluster (Figure 5a). The difference in the NND between these observed and randomized clusters indicates the degree of "nonrandomness" in rain cluster distribution. Therefore, a modified version of I_{org} $\left(I^*_{org}\right)$ can be defined as the area of actual NNCDF plotted against the NNCDF of this randomized distribution of clusters that retain the same number and sizes. This modified I^*_{org} (Figures 9e and 9f) shows that the observed clusters deviate the most from a random distribution during the decaying-to-suppressed phase of the MJO for rain clusters and during MJO enhanced-to-decaying phase for convective rain clusters.

Key identified behaviors from Figure 9 are that deep convective rain clusters rarely form in a random manner, and that their distributions become the least random during the enhanced-to-decaying phase of MJO convection. Since the number of deep convective rain clusters decreases during the decaying phase of the MJO, these results suggest two possibilities. The first is that more clustered convective cells tend to last longer, while isolated deep convective cells decay faster. The second possibility, which does not necessarily exclude the first one, is that

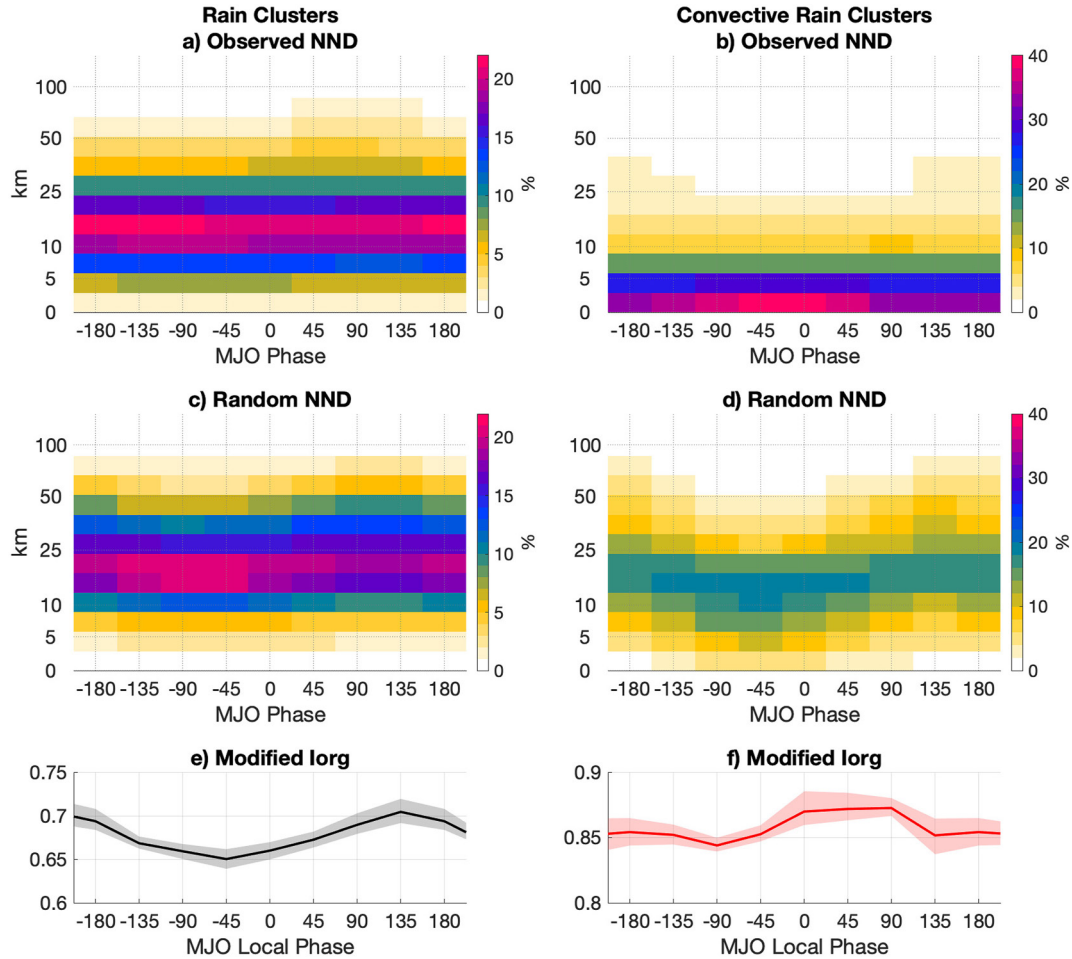

Figure 9. Probability distribution of nearest-neighboring distance of (top row) observed and (middle row) randomized clusters. The bottom row shows the modified I_{org} calculated based on the NNCDF of observed and random clusters shown in the top two rows. (left column) Rain clusters and (right column) convective rain clusters. See text for the definitions of randomized clusters and the modified I_{org}.

the generation of new convective cells is more restricted to occur within the nearby environment of preexisting convection (i.e., convection being gregarious as suggested by Mapes (1993)). Both of these behaviors would lead to continuous deviations from a random distribution during the decaying phase of the MJO.

To examine how convective systems evolve during different phases of the MJO, Figure 10 shows the evolution of stratiform rain, the intensity of convective rain, I^*_{org} (nonrandomness), the average size, and the NND of convective rain clusters relative to the time of the maximum number of convective rain clusters. These variables are regressed onto the number of convective rain clusters with time lags during different phases of the MJO, separated into its suppressed, growing, enhanced, and decaying phases. Based on the MJO local phase (Figure 1), 27 days of suppressed phase (local phase angle between 135° and −135°), 34 days of developing phases (angles between −135° and −45°), 19 days of enhanced phase (angles between −45° and 45°), and 28 days of decaying phase (angles between 45° and 135°) are identified. Regression coefficients are found using time steps when the lagged time steps are within the selected phase of the MJO. The evolutions of the regressed variables are then reconstructed using one standard deviation of the number of convective rain clusters within the selected period that is used to build the regression model. The time axis spans from 24 hr before and after the peak number in convective rain clusters, showing the evolution of convective systems on the order of their lifetime, instead of their averages on intraseasonal timescale. The evolutions of all variables show a dominant 2-day cycle, which is tied to the 2-day rain episodes observed during DYNAMO (Zuluaga & Houze, 2013). In general, as the number of deep convective rain clusters increases (Figure 10a), stratiform rain increases sharply (Figure 10b), the size of

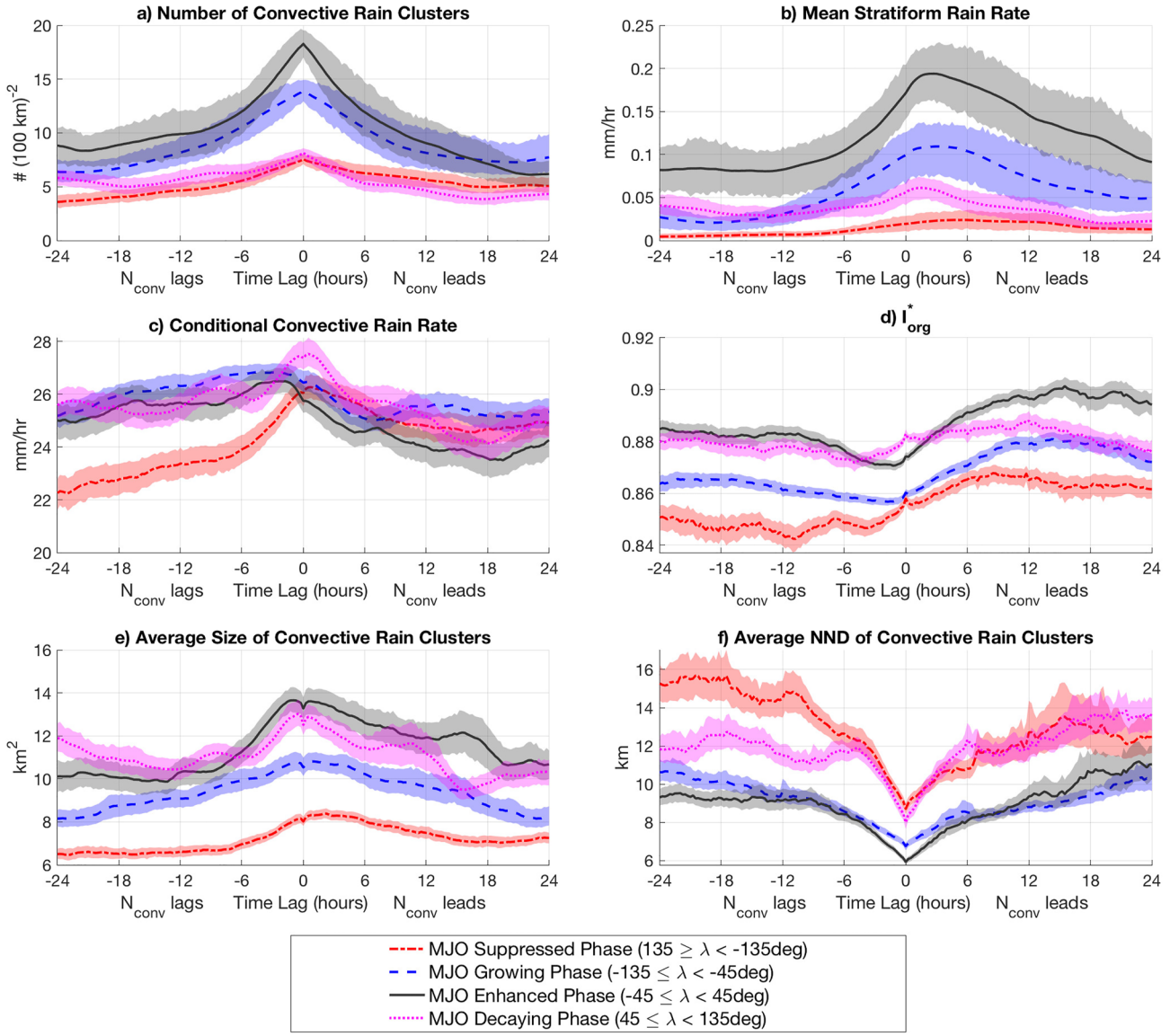

Figure 10. Time series of (a) the number density of convective rain clusters, (b) mean stratiform rain rate, (c) conditional convective rain rate, (d) modified I_{org} (I^*_{org}), (e) average size of convective rain clusters, and (f) average NND of convective rain clusters that are reconstructed using time lag regression of those quantifies onto the number density of convective rain clusters. Time lag regression was done separately during four MJO phases: suppressed (dot-dashed red), growing (dashed blue), enhanced (solid black), and decaying (dotted pink) phases. Standard deviations of the number of convective rain clusters in each MJO phase was used to reconstruct the time series.

deep convective rain clusters increases (Figure 10e), and their NND decreases (Figure 10f). However, convective cells become least randomly distributed (I^*_{org} maximizes) during the decaying phase of this 2-day rain episode, when the number of deep convective cells, their intensity, and stratiform rain are decreasing (consistent with Cheng et al., 2018). Figure 10 shows that, regardless of the large-scale environment (i.e., MJO phases), convective clusters become more organized in the 6–18 hr following the peak number of convective clusters, although some differences between MJO phases should be noted.

The average value of quantities within ±24 hr in Figure 10 shows their general evolution with the MJO, where the number of convective rain clusters and stratiform rain maximizes during the MJO enhanced phase. Within ±24 hr, the increase in the number of deep convective clusters occurs most rapidly during MJO enhanced phase, followed by the rapid increase in stratiform rain, which is expected since the detrainment of convective clouds leads to the formation of anvil clouds (Houze, 1989; Schumacher & Houze, 2003). Except for the suppressed

phase, during the different phases of the MJO, the intensity of convection (Figure 10c) remained relatively the same (the change is less than 15% of the mean), which indicates that the intensity of convection does not dominantly influence the amount of stratiform rain over the radar domain. The decaying phase of the MJO attained a relatively constant degree of nonrandomness $\left(I^*_{\text{org}}\right)$ that is higher than during MJO growing phase, although the number of deep convective cells and stratiform rain rates are smaller. However, the average NND is greater during MJO decaying than growing phase (Figure 10f). Greater I^*_{org} during MJO decaying phase indicates that the proximity of deep convective clusters is relatively higher than the expected distances between randomly distributed clusters of the same size and number. Therefore, I^*_{org} can be higher in a state of greater NND if the number of convective clusters is lower. MJO decaying phase also retains the similar size of deep convective clusters as MJO enhanced phase. These evolutions of convective properties suggest that, during MJO decaying phase, the generation of new convective cells was limited, the wide convective rain clusters persisted longer, while narrower and isolated convective clusters decayed faster, leading to the fairly persistent degree of nonrandomness $\left(I^*_{\text{org}}\right)$.

It is also important to note that the relationship between the number of convective clusters and their NND is not linear. Figure 11a shows the density distribution of the average NND of convective rain clusters plotted against their number density at each 15-min scan of the radar. The blue line in Figure 11a indicates the expected average NND of randomly distributed convective clusters of a given number density. This NND for a random distribution was generated with the same method that was used to calculate I^*_{org}. For a given number of convective rain clusters, the difference between the random and observed average NND indicates the degree of nonrandomness $\left(I^*_{\text{org}}\right)$ as demonstrated in Figure 11d. Figure 11a shows that the observed NND is always smaller than a random distribution and that there is a preferred distance between convective clusters, toward which the distribution concentrates as their number increases. This result suggests that 5–10 km is the preferred distance range at which new convection is generated relative to preexisting convection. This distance between convective clouds is consistent with the estimated distances of simulated clouds based on Figure 12 of Feng et al. (2015) and the distances between convective clouds from the RCE simulation of Torri and Kuang (2019). Prior studies show that the collision of cold pools are effective at triggering new convective clouds (Böing et al., 2012; Feng et al., 2015; Schlemmer & Hohenegger, 2014), contributing to the organization of clouds. If we assume that the cold pool fronts spread at an average of 1.78 m s^{-1} and collide within 10 min (Torri & Kuang, 2019), new clouds will form about 1 km away from the parent-convection of the cold pool. However, if we consider the time it takes for the formed clouds to deepen and precipitate (~20–30 min), through when the parent-convection can be advected by about the observed 3–5 m s^{-1} near-surface wind speed (Ruppert & Johnson, 2015), the new clouds and the parent-convection are estimated to be separated about 5–10 km as observed. Therefore, we hypothesize that cold pools play an important role in determining the distribution of convective clouds and their organization. Furthermore, Figure 11b shows that stratiform rain increases as the number of convective clusters increases and their NND decreases (Figure 11b). However, for a fixed number of convective clusters (around 10–30 per 100^2 km^2), the higher amount of stratiform rain occurs when the NND of convective clusters is smaller. The size of convective clusters generally increases with their number (Figure 11c), suggesting that the higher number density of deep convective clusters leads to their growth and formation of stratiform rain as well.

The evolution of convective rain clusters can be further diagnosed using these bivariate distributions. Figures 11e and 11f show the probability that the number of convective clusters and their NND are increasing (i.e., probability of their time tendency being positive) based on the present state of the number of convective clusters and NND. The overlaid vectors show the expected direction of evolution based on these probabilities. For example, right-pointing vectors indicate that over 50% of times the number of convective clusters increases, while downward-pointing vectors indicate that the probability of increasing NND is less than 50% (i.e., higher probability of having decreasing NND trend). These figures show that convective clusters tend to evolve from the regime with a small number of convective clusters with large NND toward the regime with a higher number and a lower NND. Once they reach a low NND of about 5 km, they tend to retain a low NND, while the number of clusters decreases, ultimately resulting in a high I^*_{org} value. This evolution of convective clusters is consistent with the evolution depicted from regression analysis in Figure 10. The cyclic evolution of convection was also shown using Gross Moist Stability (GMS; Inoue & Back, 2015) and in the relationship between precipitation and column saturation fraction (or column relative humidity; Wolding et al., 2020). These prior studies suggest that the cyclic evolution in Figure 11 between the number and NND of convective cells may be tied to the evolution of GMS and column relative humidity. The modulation of this convective cluster evolution and organization by the MJO can be understood via a "Stretched Building Block" concept by Mapes et al. (2006) where the MJO is modulating the duration,

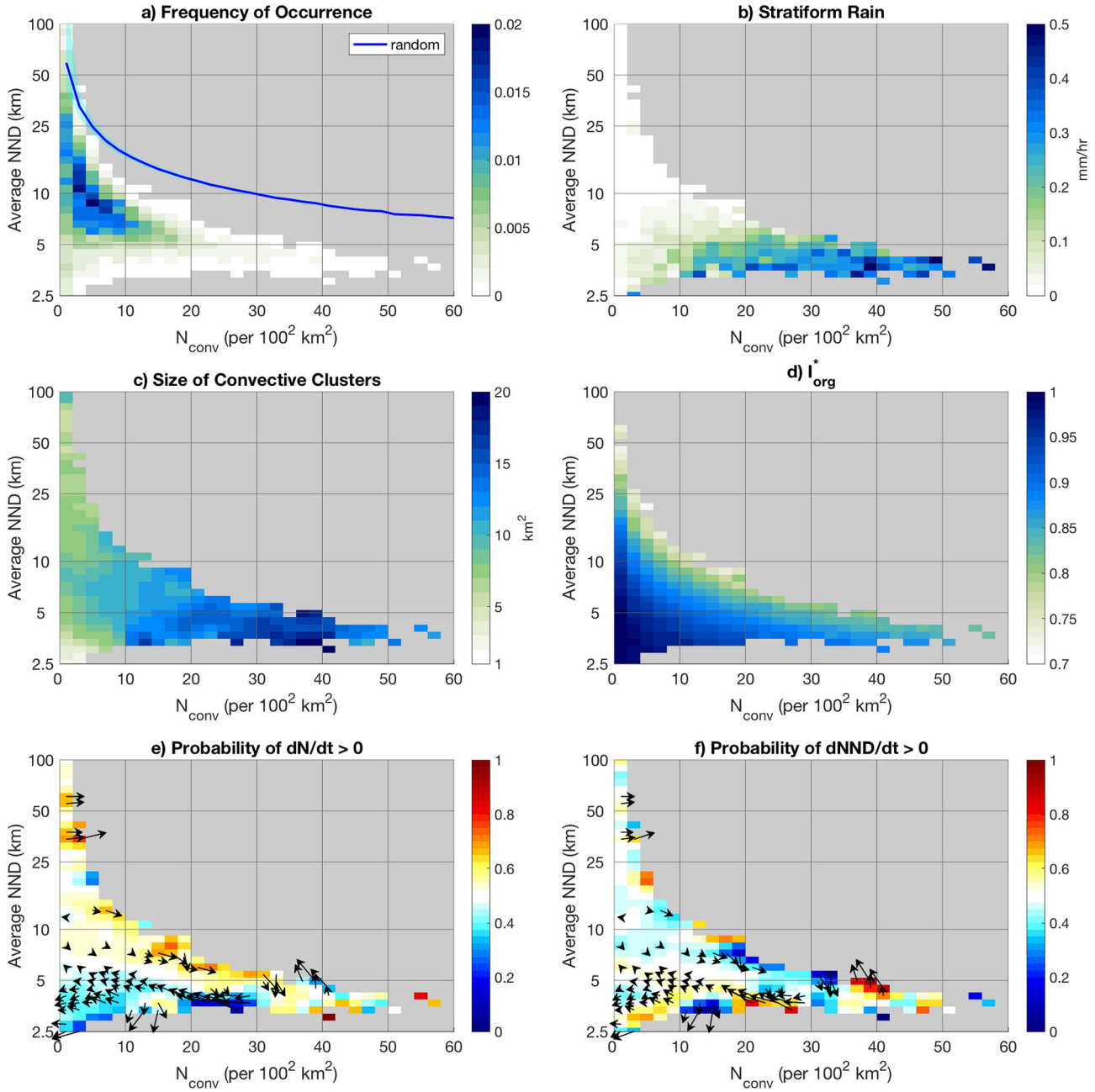

Figure 11. (a) Joint probability of the number density of convective rain clusters (N_{conv}, 100^2 km^{-2}) and their average NND (km). Blue line shows the expected NND for a random distribution. (b–d) Composites of stratiform rain (mm hr^{-1}), size of convective rain clusters (km), and modified I_{org} $\left(I^*_{org}\right)$ conditioned by the state of N_{conv} and average NND. (e, f) Shadings show the probability of positive time tendency in N_{conv} and average NND. Vectors show the direction of evolution in N_{conv} and average NND based on the probabilities (see text for more information).

frequency, and limit in the stages of convective evolution depicted in Figure 11. The enhanced MJO phase allows convective clusters to increase rapidly in number and proximity, followed by the decrease in the number while retaining their proximity. The suppressed MJO phase limits the growth in the number of convective clusters, limiting the consequent stratiform development and attainment of a state with the highly nonrandom distribution of convection. The decaying MJO phase also limits the number of convective clusters, especially isolated, scattered convection, while clustered convection embedded within decaying stratiform is retained, leading to the sustainment of the clustered and nonrandom state with a limited number of convective clusters.

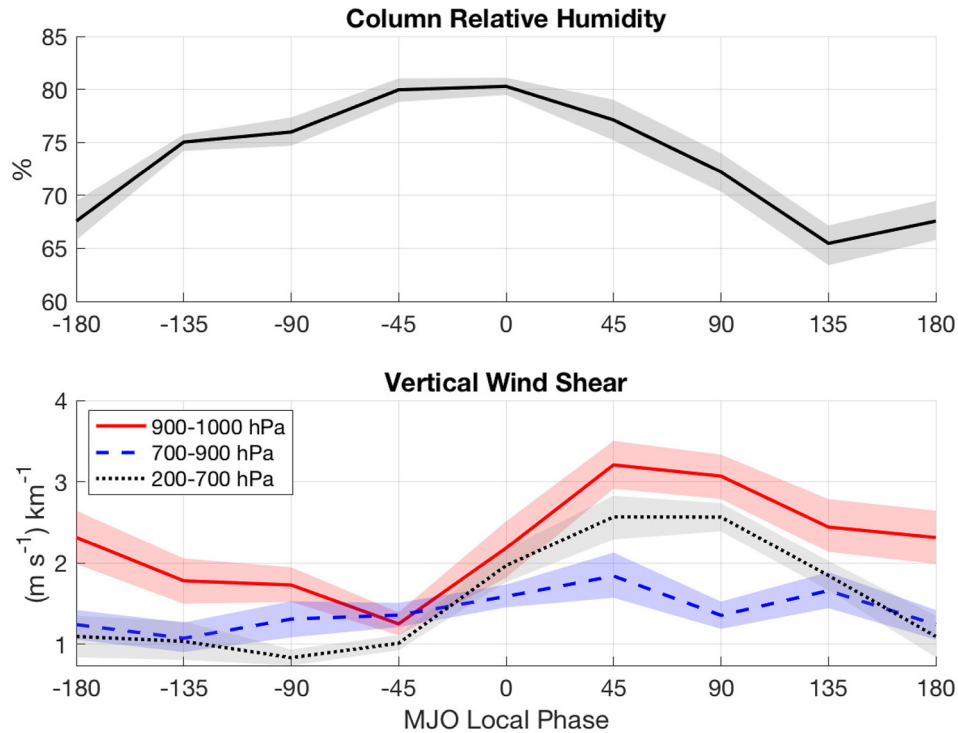

Figure 12. Composites of (a) column relative humidity and (b) vertical wind shear of horizontal wind (m s^{-1} km^{-1}) on MJO local phase. Vertical wind shear is calculated for three layers—boundary layer (900–1,000 hPa in red), free troposphere (700–900 hPa in dashed blue), and deep troposphere (200–700 hPa in dotted black).

5. Relationship Between Cloud Organization and Environmental Profiles

We will now discuss the evolution of the large-scale environment associated with the MJO to provide some hypotheses on the underlying physical mechanism of intraseasonal cloud organization. We will focus on two environmental factors that have been suggested to influence the initiation and growth of convection—the column relative humidity and vertical wind shear. Figure 12 shows the column relative humidity and vertical wind shear within the boundary layer (900–1,000 hPa), lower free troposphere (700–900 hPa), and deep troposphere (200–700 hPa). The column relative humidity is defined as the ratio of water vapor path to saturation water vapor path as in Bretherton et al. (2004) and computed within the layer from 1,000 to 200 hPa. The quantity peaks slightly before and within MJO enhanced phase at the time when the domain-averaged rainfall peaks (Figure 4a) and the rain clusters had their highest number density and size (Figures 5a and 6b). This result is consistent with the well-known relationship between column relative humidity and precipitation within the tropics (e.g., Ahmed & Schumacher, 2015; Bretherton et al., 2004; Louf et al., 2019; Schiro et al., 2020). However, the vertical shear in all layers peaks during the decaying phase of the MJO when I^*_{org} maximizes (Figures 9e and 9f). The role of vertical wind shear in supporting the clustering of convection has been suggested by many studies (Anber et al., 2014; Lamone et al., 1998; Robe & Emanuel, 2001). The effects of vertical wind shear also depend on the depth of the shear. For example, interactions between a cold pool and boundary layer shear can help generate new convective cells near preexisting convective cells, leading to clustering of convection (Rotunno et al., 1988; Schlemmer & Hohenegger, 2014; Weisman et al., 1988; Weisman & Rotunno, 2004). The effects of lower free-tropospheric shear on increasing entrainment may limit the growth of narrower clouds while convection with a wider updraft width may be less affected by entrainment and the shear can provide dynamical support to accelerate the updraft (Peters et al., 2019, 2021). Both of these effects can limit the growth of isolated convection or limit them to occur in correspondence to moist patches and leading to more clustering (Cheng et al., 2020; Torri & Kuang, 2016). Other studies also suggest that deep shear can help spread the stratiform clouds, leading to the formation of mesoscale convective systems (Lin et al., 2004). These effects of vertical wind shear at different depths may all be acting

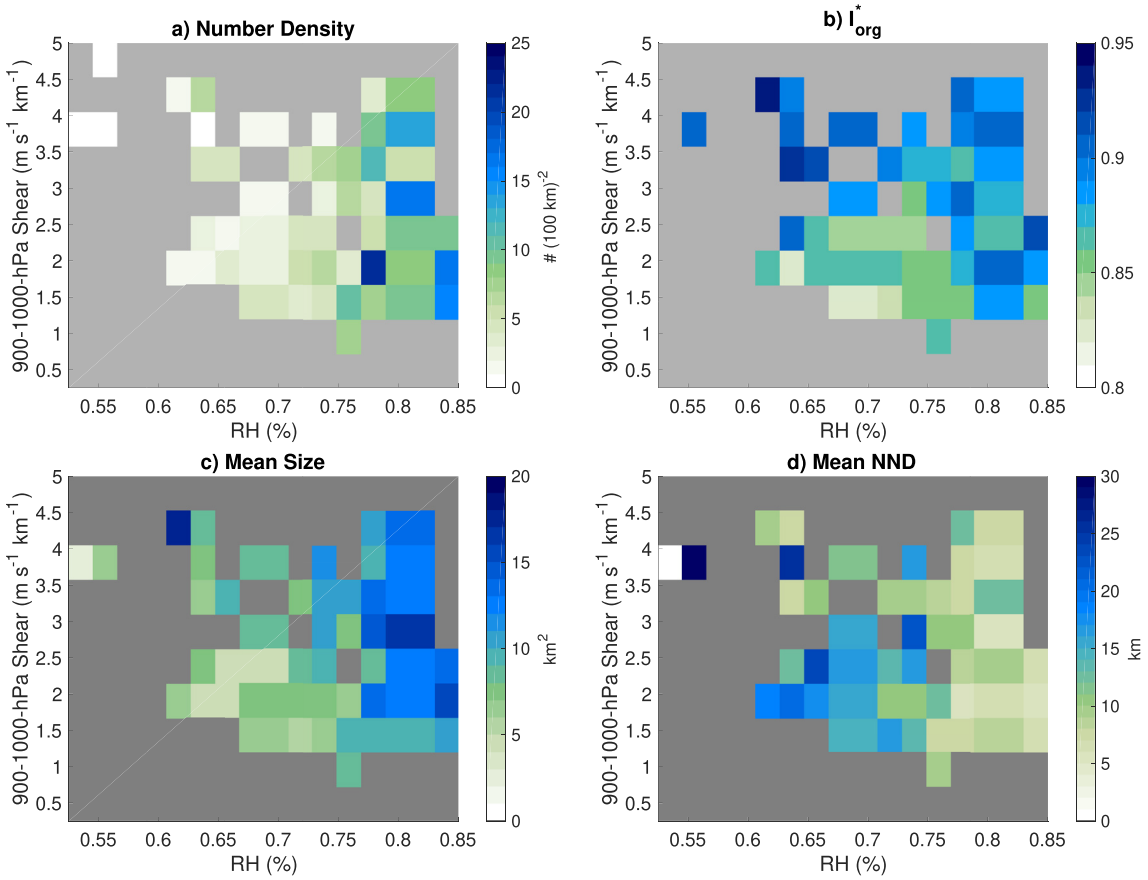

Figure 13. Average (a) number density (100^2 km^{-2}), (b) modified I_{org} $\left(I^*_{org}\right)$, (c) mean size (km^2), and (d) mean nearest-neighboring distance (NND, km) of convective rain clusters based on daily boundary layer vertical wind shear (900–1,000 hPa, m s^{-1} km^{-1}) and column relative humidity (%).

together to lead to the higher degree of nonrandomness during MJO decaying phase. Furthermore, the effect of vertical wind shear on cloud organization may depend on the environmental humidity (Anber et al., 2014).

To examine the combined effects of column humidity and vertical wind shear at different height, Figure 13 shows the average properties of convective rain clusters conditioned by the state of environmental column relative humidity and boundary layer vertical wind shear. These environmental properties were first averaged daily to eliminate the impact of the diurnal cycle. Figure 13a shows that the number density of convective rain clusters increases with column relative humidity, but it does not depend highly on the vertical wind shear. This relationship also relates to an increase in size and a decrease in NND of convective rain clusters (Figures 13c and 13d). However, the degree of nonrandomness $\left(I^*_{org}\right)$ depends more on the vertical wind shear, especially at low column relative humidity (Figure 13b). For low values of low column relative humidity, I^*_{org} appears to be more dependent on the boundary layer vertical wind shear than the shear at other depths (not shown).

These results suggest that the environmental humidity and vertical wind shear have separate effects on cloud organization. Higher environmental humidity supports the development of convection in both clustered and isolated manners by reducing the entrainment of dry air and increasing the buoyancy of air parcels. Therefore, the number of convective rain clusters increases with higher environmental humidity, while it does not necessarily lead to the highest degree of nonrandomness. Within a high humidity environment, the effects of vertical wind shear are minimal because the thermodynamic environment is already favorable for convection and any mechanical triggers (e.g., cold pool) is more likely to lead to the development of convection. On the other hand, when the environment is drier, the development of convection is more suppressed due to greater convective inhibition and reduced buoyancy of diluted parcels. This interpretation is consistent with a prior study that documented that the number of convective cells tend to decrease with higher convective inhibition (Louf et al., 2019). Therefore, we hypothesize that convection is limited to develop near preexisting convection, where detrainment and

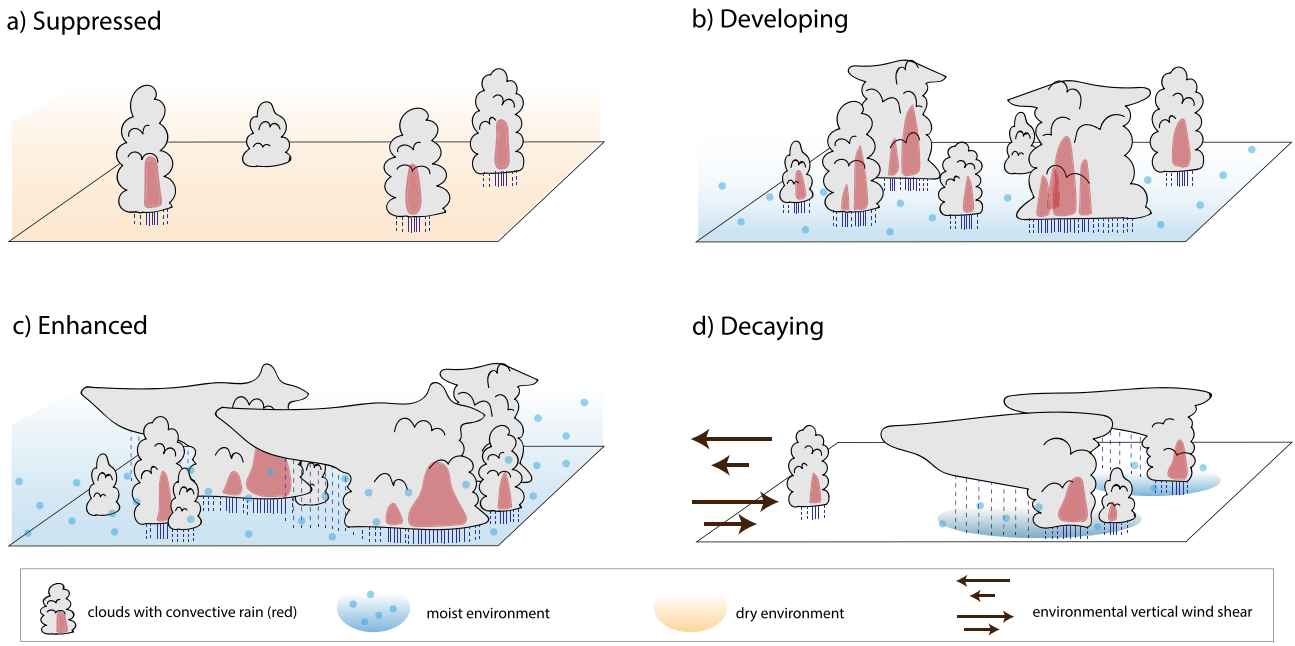

Figure 14. Schematic illustration of cloud evolution during (a) suppressed, (b) developing, (c) enhanced, and (d) decaying phase of the MJO during DYNAMO/AMIE. Red shading within clouds indicates high reflectivity associated with deep convective rain. Blue shading with dots indicates moist environment and orange shading indicates dry environment. Brown arrows show the vertical wind shear that peaked during MJO decaying phase.

precipitation create moist areas, and associated cold pools can generate new convection. This limitation in where convection can occur within the drier environment leads to higher sensitivity of clustering and nonrandomness $\left(I^*_{\text{org}}\right)$ with vertical wind shear, where the shear can provide mechanical support in the development of convection through its interactions with cold pools. These hypothesized reasons for different sensitivity to the environmental humidity and vertical wind shear at different heights will be further examined through future model experiments by the authors. We have only shown the relationships of convective properties and organization with column relative humidity and vertical wind shear, but other factors such as air-sea and cloud-radiative interactions should also be considered in future studies.

6. Summary

The objective of this study was to understand the evolution of cloud organization associated with the MJO during the DYNAMO/AMIE field campaign. We first showed that the existing five cloud organization and aggregation indices do not provide a consistent evolution in the degree of organization because the indices include different parameters and weight them differently. These cloud organization indices are also sensitive to the choice of data and variables for their calculation. Future studies that will use these indices must be aware of the underlying definition of cloud organization that was used to define each index and associated caveats (Table 1). Due to the limitations on the indices to fully understand how clouds evolve and organize with the MJO, this study examined the evolution of different parameters of convection such as their number density, size, and distances between nearest-neighboring convection with S-Polka radar.

We found that these parameters of raining clusters do not evolve simultaneously with the MJO, suggesting complexity in the definition of cloud organization. The overall evolution of cloud organization with the MJO is summarized in Figure 14. As the MJO transitions from its suppressed to enhanced phase (MJO developing phase, Figure 14b), the number of raining clusters increases and peaks slightly before the center of MJO enhanced phase. The domain-averaged rainfall also increased with the number density of raining clusters as also shown by prior studies (Barnes & Houze, 2013; Louf et al., 2019; Powell, 2019). In this study, the state of the MJO was defined using the local state of MJO-filtered OLR, leading to the lag between the peak rainfall and the center of MJO enhanced phase that is associated with minimum OLR anomalies. The increased number density of raining clusters naturally leads to increased proximity between them (reduced nearest-neighboring distances and a more

clustered state). Following the increased number and proximity of raining clusters, the sizes of both overall raining area and deep convective cells increased. This suggests that the increased number and proximity of convective cells led to the upscale growth and formation of mesoscale convective systems with broad stratiform-anvil clouds through their mergers (Figure 14c).

In addition to the evolution of the number density, size, and proximity, we also found that the spatial distribution of convective rain clusters becomes the least random during the decaying phase of the MJO when the number and size of rain clusters begin to decrease (Figure 14d). This result may be counter-intuitive to the traditional thought that organization leads to the upscale growth of convection and MCS formation. The results indicate that the important factor to upscale growth is an environment that is supportive to increasing the number and proximity of deep convection, rather than the degree of nonrandomness. While deep convection becomes less random, the physical distance between convective cells can increase when the number of deep convective cells is low, making it difficult for them to interact and merge. This intraseasonal evolution of cloud organization where deep convective clusters become less random as they decay is analogous to the evolution of 2-day rain episodes that were observed during DYNAMO (Cheng et al., 2018). Cheng et al. (2018) also separated the 2-day rain episodes into two phases. During the first phase, the number of deep convective clusters and their proximity increase. In the second phase, deep convection embedded within stratiform rain preferentially lasted or initiated while isolated deep convection was suppressed, leading to the higher state of clustering and nonrandomness. This similarity in the evolution of cloud organization between 2-day rain episodes and the MJO indicates that the large-scale environment associated with the MJO modulates the duration and frequency of different stages of shorter-timescale cloud organization (e.g., 2-day and MCSs).

The study hypothesizes that the high column relative humidity during the developing-to-enhanced phases of the MJO had contributed to the increased number of convective rain clusters. When the environment is moist, it is supportive of convective initiation and development that occur in both clustered and random (isolated) manners while the increased number of convective cells may also feedback on moistening the environment by inducing large-scale convergence and ascent. During the decaying phase of the MJO, when the environment begins to dry, our results suggest that convective development is relegated to limited areas of moist patches or nearby preexisting convection that can provide mechanical and thermodynamic forcing through its cold pools (Feng et al., 2015; Rowe & Houze, 2015; Torri & Kuang, 2016). This drying environment limits the number of convective clouds while leading to more nonrandom state. The degree of nonrandomness also appeared more sensitive to the strength of vertical wind shear when the environment is drier. Therefore, during MJO decaying phase, when the vertical wind shear maximizes in varying depths of the troposphere, the shear leads to the highest degree of nonrandomness. However, how exactly the vertical wind shear at different depths and the environmental humidity act together to influence the cloud organization remains to be understood.

Data Availability Statement

The DYNAMO/AMIE data used in this work were obtained from DYNAMO Legacy website (http://dynamo.fl-ext.ucar.edu/rsmas/dynamo_legacy/; Johnson et al., 2018; Rutledge et al., 2018). NOAA Interpolated OLR is available from NOAA Physical Sciences Laboratory website (https://psl.noaa.gov/data/gridded/data.interp_OLR.html; Liebmann & Smith, 1996). NOAA NCEP/NPC merged IR brightness temperature data were obtained from NASA Earthdata (https://disc.gsfc.nasa.gov/datasets/GPM_MERGIR_1/summary; Janowiak et al., 2017).

Acknowledgments
We acknowledge the support of this work by Department of Energy Atmospheric System Program funding DE-SC0020188. We thank three anonymous reviewers for their comments to help improve this manuscript.

References

Ahmed, F., & Schumacher, C. (2015). Convective and stratiform components of the precipitation-moisture relationship. *Geophysical Research Letters*, *42*, 10453–10462. https://doi.org/10.1002/2015GL066957

Anber, U., Wang, S., & Sobel, A. (2014). Response of atmospheric convection to vertical wind shear: Cloud-system-resolving simulations with parameterized large-scale circulation. Part I: Specified radiative cooling. *Journal of the Atmospheric Sciences*, *71*(8), 2976–2993. https://doi.org/10.1175/jas-d-13-0320.1

Barnes, H. C., & Houze, R. A. (2013). The precipitating cloud population of the Madden-Julian Oscillation over the Indian and west Pacific oceans. *Journal of Geophysical Research: Atmospheres*, *118*, 6996–7023. https://doi.org/10.1002/jgrd.50375

Benedict, J. J., & Randall, D. A. (2007). Observed characteristics of the MJO relative to maximum rainfall. *Journal of the Atmospheric Sciences*, *64*(7), 2332–2354. https://doi.org/10.1175/jas3968.1

Böing, S. J., Jonker, H. J. J., Siebesma, A. P., & Grabowski, W. W. (2012). Influence of the subcloud layer on the development of a deep convective ensemble. *Journal of the Atmospheric Sciences*, *69*(9), 2682–2698. https://doi.org/10.1175/JAS-D-11-0317.1

Bretherton, C. S., McCaa, J. R., & Grenier, H. (2004). A new parameterization for shallow cumulus convection and its application to marine subtropical cloud-topped boundary layers. Part I: Description and 1d results. *Monthly Weather Review*, *132*(4), 864–882. https://doi.org/10.1175/1520-0493(2004)132<0864:ANPFSC>2.0.CO;2

Chen, B., & Mapes, B. E. (2018). Effects of a simple convective organization scheme in a two-plume GCM. *Journal of Advances in Modeling Earth Systems*, *10*, 867–880. https://doi.org/10.1002/2017MS001106

Cheng, W.-Y., Kim, D., & Rowe, A. (2018). Objective quantification of convective clustering observed during the AMIE/DYNAMO two-day rain episodes. *Journal of Geophysical Research: Atmospheres*, *123*, 10361–10378. https://doi.org/10.1029/2018JD028497

Cheng, W.-Y., Kim, D., Rowe, A., Moon, Y., & Wang, S. (2020). Mechanisms of convective clustering during a 2-day rain event in AMIE/DYNAMO. *Journal of Advances in Modeling Earth Systems*, *12*, e2019MS001907. https://doi.org/10.1029/2019MS001907

Ciesielski, P. E., Johnson, R. H., Jiang, X., Zhang, Y., & Xie, S. (2017). Relationships between radiation, clouds, and convection during DYNAMO. *Journal of Geophysical Research: Atmospheres*, *122*, 2529–2548. https://doi.org/10.1002/2016JD025965

Ciesielski, P. E., Yu, H., Johnson, R. H., Yoneyama, K., Katsumata, M., Long, C. N., et al. (2014). Quality-controlled upper-air sounding dataset for DYNAMO/CINDY/AMIE: Development and corrections. *Journal of Atmospheric and Oceanic Technology*, *31*(4), 741–764. https://doi.org/10.1175/jtech-d-13-00165.1

Del Genio, A. D., & Chen, Y. (2015). Cloud-radiative driving of the Madden-Julian oscillation as seen by the A-Train. *Journal of Geophysical Research: Atmospheres*, *120*, 5344–5356. https://doi.org/10.1002/2015JD023278

Dolan, B., Hein, P., Rutledge, S., & Powell, S. (2017). *DYNAMO legacy rainfall products*. Retrieved from https://orca.atmos.washington.edu/dynamo_legacy/resources/documents/readme/radar/radar_spolka_readme.pdf

Feng, Z., Hagos, S., Rowe, A. K., Burleyson, C. D., Martini, M. N., & deSzoeke, S. P. (2015). Mechanisms of convective cloud organization by cold pools over tropical warm ocean during the AMIE/dynamo field campaign. *Journal of Advances in Modeling Earth Systems*, *7*, 1942–2466. https://doi.org/10.1002/2014MS000384

Genio, A. D. D., Chen, Y., Kim, D., & Yao, M.-S. (2012). The MJO transition from shallow to deep convection in Cloudsat/Calipso data and GISS GCM simulations. *Journal of Climate*, *25*(11), 3755–3770. https://doi.org/10.1175/JCLI-D-11-00384.1

Holloway, C. E., & Neelin, J. D. (2009). Moisture vertical structure, column water vapor, and tropical deep convection. *Journal of the Atmospheric Sciences*, *66*(6), 1665–1683. https://doi.org/10.1175/2008jas2806.1

Houze, R. A. (1989). Observed structure of mesoscale convective systems and implications for large-scale heating. *Quarterly Journal of the Royal Meteorological Society*, *115*(487), 425–461. https://doi.org/10.1002/qj.49711548702

Inoue, K., & Back, L. (2015). Column-integrated moist static energy budget analysis on various time scales during TOGA COARE. *Journal of the Atmospheric Sciences*, *72*(5), 1856–1871. https://doi.org/10.1175/jas-d-14-0249.1

Janowiak, J., Joyce, B., & Xie, P. (2017). NCEP/CPC L3 half hourly 4km global (60S-60N) merged IR V1 (Tech. Rep.). [Data Set]. *Goddard Earth Sciences Data and Information Services Center (GES DISC)*.

Johnson, R., Schubert, W., Taft, R., & Ciesielski, P. (2018). DYNAMO atmospheric sounding data and products. [Data Set]. *UCAR Earth Observing Laboratory*. Retrieved from https://orca.atmos.washington.edu/dynamo_legacy/resources/documents/readme/soundings/soundings_readme.pdfdataset

Kadoya, T., & Masunaga, H. (2018). New observational metrics of convective self-aggregation: Methodology and a case study. *Journal of the Meteorological Society of Japan. Series II*, *96*(6), 535–548. https://doi.org/10.2151/jmsj.2018-054

Kikuchi, K., & Takayabu, Y. N. (2004). The development of organized convection associated with the MJO during TOGA COARE IOP: Trimodal characteristics. *Geophysical Research Letters*, *31*, L10101. https://doi.org/10.1029/2004GL0196012004

Kiladis, G. N., Dias, J., Straub, K. H., Wheeler, M. C., Tulich, S. N., Kikuchi, K., et al. (2014). A comparison of OLR and circulation-based indices for tracking the MJO. *Monthly Weather Review*, *142*(5), 1697–1715. https://doi.org/10.1175/MWR-D-13-00301.1

Kiladis, G. N., Straub, K. H., & Haertel, P. T. (2005). Zonal and vertical structure of the Madden-Julian oscillation. *Journal of the Atmospheric Sciences*, *62*(8), 2790–2809. https://doi.org/10.1175/JAS3520.1

Lamone, M. A., Zipser, E. J., & Trier, S. B. (1998). The role of environmental shear and thermodynamic conditions in determining the structure and evolution of mesoscale convective systems during TOGA COARE. *Journal of the Atmospheric Sciences*, *55*(23), 3493–3518.

Liebmann, B., & Smith, C. A. (1996). Description of a complete (interpolated) outgoing long-wave radiation dataset. *Bulletin of the American Meteorological Society*, *77*, 1275–1277.

Lin, J., Mapes, B., Zhang, M., & Newman, M. (2004). Stratiform precipitation, vertical heating profiles, and the Madden-Julian oscillation. *Journal of the Atmospheric Sciences*, *61*(3), 296–309. https://doi.org/10.1175/1520-0469(2004)061<0296:SPVHPA>2.0.CO;2

Louf, V., Jakob, C., Protat, A., Bergemann, M., & Narsey, S. (2019). The relationship of cloud number and size with their large-scale environment in deep tropical convection. *Geophysical Research Letters*, *46*, 9203–9212. https://doi.org/10.1029/2019GL083964

Madden, R. A., & Julian, P. R. (1994). Observations of the 40–50-day tropical oscillation. *Monthly Weather Review*, *112*, 814–837. https://doi.org/10.1175/1520-0493(1994)122<0814:OOTDTO>2.0.CO;2

Mapes, B. (1993). Gregarious tropical convection. *Journal of the Atmospheric Sciences*, *50*(13), 2026–2037. https://doi.org/10.1175/1520-0469(1993)050<2026:GTC>2.0.CO;2

Mapes, B., Tulich, S., Lin, J., & Zuidema, P. (2006). The mesoscale convection life cycle: Building block or prototype for large-scale tropical waves? *Dynamics of Atmospheres and Oceans*, *42*(1), 3–29. https://doi.org/10.1016/j.dynatmoce.2006.03.003

Moncrieff, M. W. (2019). Toward a dynamical foundation for organized convection parameterization in GCMS. *Geophysical Research Letters*, *46*, 14103–14108. https://doi.org/10.1029/2019GL085316

Muller, C., & Bony, S. (2015). What favors convective aggregation and why? *Geophysical Research Letters*, *42*, 5626–5634. https://doi.org/10.1002/2015GL064260

Nair, U. S., Weger, R. C., Kuo, K. S., & Welch, R. M. (1998). Clustering, randomness, and regularity in cloud fields: 5. The nature of regular cumulus cloud fields. *Journal of Geophysical Research*, *103*(D10), 11363–11380. https://doi.org/10.1029/98JD00088

Peters, J. M., Morrison, H., Zhang, G. J., & Powell, S. W. (2021). Improving the physical basis for updraft dynamics in deep convection parameterizations. *Journal of Advances in Modeling Earth Systems*, *13*, e2020MS002282. https://doi.org/10.1029/2020MS002282

Peters, J. M., Nowotarski, C. J., & Morrison, H. (2019). The role of vertical wind shear in modulating maximum supercell updraft velocities. *Journal of the Atmospheric Sciences*, *76*(10), 3169–3189. https://doi.org/10.1175/JAS-D-19-0096.1

Powell, S. W. (2019). Observing possible thermodynamic controls on tropical marine rainfall in moist environments. *Journal of the Atmospheric Sciences*, *76*(12), 3737–3751. https://doi.org/10.1175/JAS-D-19-0144.1

Powell, S. W., & Houze, R. A. (2015). Evolution of precipitation and convective echo top heights observed by TRMM radar over the Indian Ocean during DYNAMO. *Journal of Geophysical Research: Atmospheres*, *120*, 3906–3919. https://doi.org/10.1002/2014JD022934

Powell, S. W., RobertHouze, A. J., & Brodzik, S. R. (2016). Rainfall-type categorization of radar echoes using polar coordinate reflectivity data. *Journal of Atmospheric and Oceanic Technology*, *33*(3), 523–538. https://doi.org/10.1175/jtech-d-15-0135.1

Randall, D., Khairoutdinov, M., Arakawa, A., & Grabowski, W. (2003). Breaking the cloud parameterization deadlock. *Bulletin of the American Meteorological Society*, *84*(11), 1547–1564. https://doi.org/10.1175/BAMS-84-11-1547

Retsch, M. H., Jakob, C., & Singh, M. S. (2020). Assessing convective organization in tropical radar observations. *Journal of Geophysical Research: Atmospheres*, *125*, e2019JD031801. https://doi.org/10.1029/2019JD031801

Riley, E. M., Mapes, B. E., & Tulich, S. N. (2011). Clouds associated with the Madden-Julian oscillation: A new perspective from CloudSat. *Journal of the Atmospheric Sciences*, *68*(12), 3032–3051. https://doi.org/10.1175/jas-d-11-030.1

Robe, F. R., & Emanuel, K. A. (2001). The effect of vertical wind shear on radiative–convective equilibrium states. *Journal of the Atmospheric Sciences*, *58*(11), 1427–1445. https://doi.org/10.1175/1520-0469(2001)058<1427:TEOVWS>2.0.CO;2

Rotunno, R., Klemp, J. B., & Weisman, M. L. (1988). A theory for strong, long-lived squall lines. *Journal of the Atmospheric Sciences*, *45*(3), 463–485. https://doi.org/10.1175/1520-0469(1988)045<0463:ATFSLL>2.0.CO;2

Rowe, A. K., & Houze, R. A. (2015). Cloud organization and growth during the transition from suppressed to active MJO conditions. *Journal of Geophysical Research: Atmospheres*, *120*, 2169–8996. https://doi.org/10.1002/2014JD022948

Ruppert, J. H., & Johnson, R. H. (2015). Diurnally modulated cumulus moistening in the preonset stage of the Madden-Julian oscillation during DYNAMO. *Journal of the Atmospheric Sciences*, *72*(4), 1622–1647. https://doi.org/10.1175/jas-d-14-0218.1

Rutledge, S., Hein, P., Dolan, B., Powell, S., & Brodzik, S. (2018). NCAR S-polka radar data: DYNAMO legacy data products. [Data Set]. UCAR Earth Observing Laboratory. Retrieved from https://orca.atmos.washington.edu/dynamo_legacy/resources/documents/readme/radar/radar_spolka_readme.pdf

Sakaeda, N., Dias, J., & Kiladis, G. N. (2020). The diurnal cycle of rainfall and the convectively-coupled equatorial waves over the Maritime Continent. *Journal of Climate*, *33*(8), 3307–3331. https://doi.org/10.1175/jcli-d-19-0043.1

Schiro, K. A., Sullivan, S. C., Kuo, Y.-H., Su, H., Gentine, P., Elsaesser, G. S., & Neelin, J. D. (2020). Environmental controls on tropical mesoscale convective system precipitation intensity. *Journal of the Atmospheric Sciences*, *77*(12), 4233–4249. https://doi.org/10.1175/JAS-D-20-0111.1

Schlemmer, L., & Hohenegger, C. (2014). The formation of wider and deeper clouds as a result of cold-pool dynamics. *Journal of the Atmospheric Sciences*, *71*(8), 2842–2858. https://doi.org/10.1175/JAS-D-13-0170.1

Schumacher, C., & Houze, R. A. (2003). Stratiform rain in the tropics as seen by the TRMM precipitation radar. *Journal of Climate*, *16*(11), 1739–1756. https://doi.org/10.1175/1520-0442(2003)016<1739:SRITTA>2.0.CO;2

Thompson, E. J., Rutledge, S. A., Dolan, B., Thurai, M., & Chandrasekar, V. (2018). Dual-polarization radar rainfall estimation over tropical oceans. *Journal of Applied Meteorology and Climatology*, *57*(3), 755–775. https://doi.org/10.1175/JAMC-D-17-0160.1

Tobin, I., Bony, S., & Roca, R. (2012). Observational evidence for relationships between the degree of aggregation of deep convection, water vapor, surface fluxes, and radiation. *Journal of Climate*, *25*(20), 6885–6904. https://doi.org/10.1175/JCLI-D-11-00258.1

Tompkins, A. M., & Semie, A. G. (2017). Organization of tropical convection in low vertical wind shears: Role of updraft entrainment. *Journal of Advances in Modeling Earth Systems*, *9*, 1046–1068. https://doi.org/10.1002/2016MS000802

Torri, G., & Kuang, Z. (2016). Rain evaporation and moist patches in tropical boundary layers. *Geophysical Research Letters*, *43*, 9895–9902. https://doi.org/10.1002/2016GL070893

Torri, G., & Kuang, Z. (2019). On cold pool collisions in tropical boundary layers. *Geophysical Research Letters*, *46*, 399–407. https://doi.org/10.1029/2018GL080501

Torri, G., Kuang, Z., & Tian, Y. (2015). Mechanisms for convection triggering by cold pools. *Geophysical Research Letters*, *42*, 1943–1950. https://doi.org/10.1002/2015GL063227

Weger, R. C., Lee, J., Zhu, T., & Welch, R. M. (1992). Clustering, randomness and regularity in cloud fields: 1. Theoretical considerations. *Journal of Geophysical Research*, *97*(D18), 20519–20536. https://doi.org/10.1029/92JD02038

Weisman, M. L., Klemp, J. B., & Rotunno, R. (1988). Structure and evolution of numerically simulated squall lines. *Journal of the Atmospheric Sciences*, *45*(14), 1990–2013. https://doi.org/10.1175/1520-0469(1988)045<1990:SAEONS>2.0.CO;2

Weisman, M. L., & Rotunno, R. (2004). "A theory for strong long-lived squall lines" revisited. *Journal of the Atmospheric Sciences*, *61*(4), 361–382. https://doi.org/10.1175/1520-0469(2004)061<0361:ATFSLS>2.0.CO;2

Wheeler, M. C., & Hendon, H. H. (2004). An all-season real-time multivariate MJO index: Development of an index for monitoring and prediction. *Monthly Weather Review*, *132*(8), 1917–1932. https://doi.org/10.1175/1520-0493(2004)132<1917:AARMMI>2.0.CO;2

Wheeler, M. C., & Kiladis, G. (1999). Convectively-coupled equatorial waves: Analysis of clouds in the wavenumber-frequency domain. *Journal of the Atmospheric Sciences*, *56*, 374–399. https://doi.org/10.1175/1520-0469(1999)056<0374:CCEWAO>2.0.CO;2

White, B. A., Buchanan, A. M., Birch, C. E., Stier, P., & Pearson, K. J. (2018). Quantifying the effects of horizontal grid length and parameterized convection on the degree of convective organization using a metric of the potential for convective interaction. *Journal of the Atmospheric Sciences*, *75*(2), 425–450. https://doi.org/10.1175/JAS-D-16-0307.1

Wing, A. A., & Emanuel, K. A. (2014). Physical mechanisms controlling self-aggregation of convection in idealized numerical modeling simulations. *Journal of Advances in Modeling Earth Systems*, *6*, 59–74. https://doi.org/10.1002/2013MS000269

Wing, A., Emanuel, K., Holloway, C., & Muller, C. (2017). Shallow clouds, water vapor, circulation, and climate sensitivity. In R.Pincus, W. D., S.Bony, & B.Stevens (Eds.), Convective self-*aggregation in numerical simulations: A review*(Vol. 65). Springer, .

Wolding, B., Dias, J., Kiladis, G., Ahmed, F., Powell, S. W., Maloney, E., & Branson, M. (2020). Interactions between moisture and tropical convection. part i: The coevolution of moisture and convection. *Journal of the Atmospheric Sciences*, *77*(5), 1783–1799. https://doi.org/10.1175/JAS-D-19-0225.1

Wolding, B., Maloney, E., & Branson, M. (2016). Vertically resolved weak temperature gradient analysis of the Madden-Julian Oscillation in SP-CESM. *Journal of Advances in Modeling Earth Systems*, *8*, 1586–1619. https://doi.org/10.1002/2016MS000724

Xu, W., & Rutledge, S. A. (2015). Morphology, intensity, and rainfall production of MJO convection: Observations from DYNAMO shipborne radar and TRMM. *Journal of the Atmospheric Sciences*, *72*(2), 623–640. https://doi.org/10.1175/jas-d-14-0130.1

Xu, W., Rutledge, S. A., Schumacher, C., & Katsumata, M. (2015). Evolution, properties, and spatial variability of MJO convection near and off the equator during DYNAMO. *Journal of the Atmospheric Sciences*, *72*(11), 4126–4147. https://doi.org/10.1175/jas-d-15-0032.1

Yang, Q., Majda, A. J., & Moncrieff, M. W. (2019). Upscale impact of mesoscale convective systems and its parameterization in an idealized GCM for an MJO analog above the equator. *Journal of the Atmospheric Sciences*, *76*(3), 865–892. https://doi.org/10.1175/JAS-D-18-0260.1

Yasunaga, K., & Mapes, B. (2011). Differences between more divergent and more rotational types of convectively coupled equatorial waves. Part I: Space–time spectral analyses. *Journal of the Atmospheric Sciences*, *69*(1), 3–16. https://doi.org/10.1175/JAS-D-11-033.1

Yoneyama, K., Zhang, C., & Long, C. N. (2013). Tracking pulses of the Madden-Julian oscillation. *Bulletin of the American Meteorological Society*, *94*(12), 1871–1891. https://doi.org/10.1175/bams-d-12-00157.1

Zuluaga, M. D., & Houze, R. A. (2013). Evolution of the population of precipitating convective systems over the equatorial Indian ocean in active phases of the Madden-Julian Oscillation. *Journal of the Atmospheric Sciences*, *70*(9), 2713–2725. https://doi.org/10.1175/jas-d-12-0311.1